

RESEARCH ARTICLE

10.1002/2014JD021664

Key Point:

- V-shaped GWs are observed after a fireball meteor. Modeled GWs look similar

Supporting Information:

- Readme
- Movie S1

Correspondence to:

S. L. Vadas,
vasha@cora.nwra.com

Citation:

Vadas, S. L., H. Suzuki, M. J. Nicolls, T. Nakamura, and R. O. Harmon (2014), Atmospheric gravity waves excited by a fireball meteor: Observations and modeling, *J. Geophys. Res. Atmos.*, 119, doi:10.1002/2014JD021664.

Received 20 FEB 2014

Accepted 20 JUN 2014

Accepted article online 24 JUN 2014

Atmospheric gravity waves excited by a fireball meteor: Observations and modeling

Sharon L. Vadas¹, Hidehiko Suzuki², Michael J. Nicolls³, Takuji Nakamura⁴, and Robert O. Harmon⁵

¹NWRA/CoRA office, Boulder, Colorado, USA, ²Department of Physics, Meiji University, Kawasaki, Japan, ³Center for Geospace Studies, SRI International, Menlo Park, California, USA, ⁴National Institute of Polar Research, Tachikawa, Japan, ⁵Physics and Astronomy, Ohio Wesleyan University, Delaware, Ohio, USA

Abstract In a companion paper, Suzuki et al. (2013) studied an expanding circular train observed in the Na airglow for 9 min above Syowa Station, Antarctica, on 7 June 2008. This train was created by a southwestward moving fireball meteor. Here we report on “V”-shaped faint gravity waves (GWs) partially visible in many of the Na airglow images 8 to 43 min after the meteor. The GW phase lines appear to originate from the horizontal projection of the meteor path, with angles -42 to -52° south and 10 to 20° north of the path. The GWs south of the path propagated southwestward with a horizontal phase speed of $c_H \sim 80$ – 100 m/s, while those north of the path propagated northwestward with $c_H \sim 20$ – 40 m/s. Those south (north) of the path had horizontal wavelengths $\lambda_H \sim 25$ – 35 km ($\lambda_H \sim 18$ km) and periods $\tau_r \sim 5$ – 6 min ($\tau_r \sim 7$ – 15 min). We then model the GWs excited by idealized horizontal and slanted heatings and body forces. We show that the GW phase lines form Vs when the heat/force is slanted vertically. If the central altitude of the heat/force is $z_0 > 92$ km, the open ends of the Vs are mainly directed away from the meteor trajectory. If the heat/force is long enough, two oppositely directed Vs are created, forming an “X” at the center of the structure. We find that λ_H depends sensitively on the width of the heating. We obtain heating parameters which compare reasonably well with the Na observations: $z_0 \sim 120$ km, half-length half maximum of ~ 25 – 35 km, and half width half maximum of ~ 2 – 3 km.

1. Introduction

The air in the Earth's atmosphere is composed primarily of monatomic and diatomic molecules. From the lower atmosphere to the upper thermosphere, these molecules can be described as a fluid, since sufficient interactions occur between the molecules. It is well known that heat/coolings and body forces excite gravity waves (GWs) [Zhu and Holton, 1987; Alexander et al., 1995; Walterscheid et al., 2001; Vadas and Fritts, 2001]. Using a heating/forcing which turns on and off smoothly in time, it was shown theoretically that the forcing duration must be of the order of or shorter than its characteristic time in order to excite GWs with significant amplitudes [Vadas and Fritts, 2001]. Here the characteristic time is obtained by plugging the length scales of the heating/forcing into the GW dispersion relation. Heating/forcing durations much longer than this characteristic time create long-period GWs with small amplitudes.

The theoretical solutions derived in Vadas and Fritts [2001] were obtained using the Boussinesq approximation, a formalism which inherently eliminates acoustic waves (AWs) from the solution. This is a good approximation for fluid motions with velocities that are much slower than the sound speed. However, when these motions are rapid (such as might occur after a fireball meteor burns up in our atmosphere), the AW response is expected to be significant. In such cases, the compressible solutions are necessary. Recently, these Boussinesq solutions were generalized to include compressibility in full, thereby allowing for the determination of both the AWs and GWs excited by heatings and forcings [Vadas, 2013]. Note that the Boussinesq solutions can be used to describe the GWs adequately if $\lambda_z \ll 2\pi H$, where λ_z is the GW vertical wavelength and H is the density scale height. However, if $\lambda_z > \pi H$, the compressible solutions must be used to correctly calculate the GW amplitudes [Vadas, 2013].

One well-known example of a heating which excites GWs in the lower stratosphere is deep convection [e.g., Holton and Alexander, 1999]. Another well-known example is the aurora, which excites GWs at $z \sim 120$ – 150 km in the thermosphere [Richmond, 1978; Hocke and Schlegel, 1996]. Additionally, AWs and GWs are excited at the locations where fireball meteors interact with the Earth's atmosphere [Revelle, 1976; Cepelcha et al., 1998]. This tends to occur in the MLT (mesosphere and lower thermosphere) region.

Recently, Na airglow observations captured a fireball meteor as it entered the Earth's atmosphere over Syowa Station, Antarctica, on 7 June 2008 at 21:58:45 UT [Suzuki *et al.*, 2013]. Directly afterward, a luminous train was observed in the Na airglow. This train became circular and expanded rapidly in time over 9 min. Since the (x, y) path of the meteor was well known, and because the meteor emitted sodium, the motion of the train was used to deduce the background wind in the upper mesosphere at $z \sim 76\text{--}87$ km. This background wind consisted of a mean plus an inertia-gravity wave with a vertical wavelength of $\lambda_z \sim 16$ km and a horizontal wind amplitude of ~ 30 m/s.

Although not discussed in Suzuki *et al.* [2013], waves with a "V"-shaped structure were also observed in the Na airglow 8 to 43 min after this meteor. The phase lines of these waves appeared to originate from the meteor trajectory. Unfortunately, most of these waves were faint because they were observed with an all-sky camera with a limited aperture.

The purpose of this companion paper is to (1) present the Na airglow images containing these waves, (2) determine their properties and show that they are GWs, and (3) understand the origin and properties of these GWs via targeted modeling studies. In section 2, we discuss the properties of the meteor. We also discuss our image-processing method and show the Na airglow images containing these waves. We determine the horizontal wavelengths, phase speeds, and periods of these waves in section 3. In section 4, we present idealized modeling results for horizontal and slanted line-shaped heatings and three-dimensional (3-D) body forces. Section 5 contains a discussion of the heating caused by meteor fireballs, and section 6 contains our conclusions.

2. Observations of the Fireball Meteor and Na Airglow Images

2.1. Trajectory of the Fireball Meteor

On 7 June 2008, a fireball meteor was observed at 21:58:45 UT over Syowa Station in the Antarctica by an all-sky television camera (ATV) [Suzuki *et al.*, 2013]. The ATV is a panoramic, white-light all-sky TV camera which records aurora morphology at a frame rate of 30 s^{-1} . Figure 1a shows the path of this meteor from the northeast to the northwest of Syowa Station as determined from the ATV. Here x and y are the zonal and meridional directions, respectively, and Syowa Station is located at $x = y = 0$. The direction of propagation of the meteor was $180^\circ + \theta_{\text{meteor}} = 197.1^\circ$ counterclockwise from east, where $\theta_{\text{meteor}} = 17.1^\circ$. Additionally, its angle from the horizontal plane was $\psi_{\text{meteor}} = -28.5^\circ$; therefore, it moved nearly horizontally. Although the meteor's angle within the horizontal plane is known well, its altitude above Syowa Station is somewhat uncertain because there was only a single ATV camera. An assumed altitude was adopted in Suzuki *et al.* [2013] which we utilize here. Using this assumed altitude, the meteor's geocentric velocity was determined to be 69 ± 1 km/s.

We rotate our coordinate system counterclockwise by $\theta = 17.1^\circ$ into a coordinate frame which is aligned with the meteor trajectory:

$$x' = x \cos \theta + y \sin \theta, \quad y' = -x \sin \theta + y \cos \theta. \quad (1)$$

Figure 1b shows the meteor's path as a function of x' and the assumed altitude (left axis) and the zwd (or "zero-wind-deduced") altitude (right axis). Here the zwd altitude is 17 km higher than the assumed altitude (see section 4.1.2).

Figure 1c shows the number of counts for the meteor as observed by the ATV, n_{meteor} . The meteor was easily visible from $z \sim 110$ to 75 km. The number of counts is maximum at $z \sim 88$ km.

2.2. Luminosity of the Fireball Meteor

To estimate the luminosity profile of the meteor, we divide the number of meteor counts by the number of counts from an astronomical object of known brightness that also appears in the images. Ideally, we would use the brightest object for this comparison. The brightest object here (other than the meteor) is the planet Jupiter, for which the mean number of counts after subtracting the background is $n_{\text{Jupiter}} = 5987$. However, the analysis is complicated by the following:

1. The camera optics illuminate the center of the field better than the edges ("vignetting"). As a result, objects farther from the zenith will look dimmer than they should relative to objects close to the zenith.
2. The greater the angle between an object and the zenith, the greater the path length for light reaching the camera. Thus, absorption and scattering by the atmosphere produces greater dimming for objects farther from the zenith.

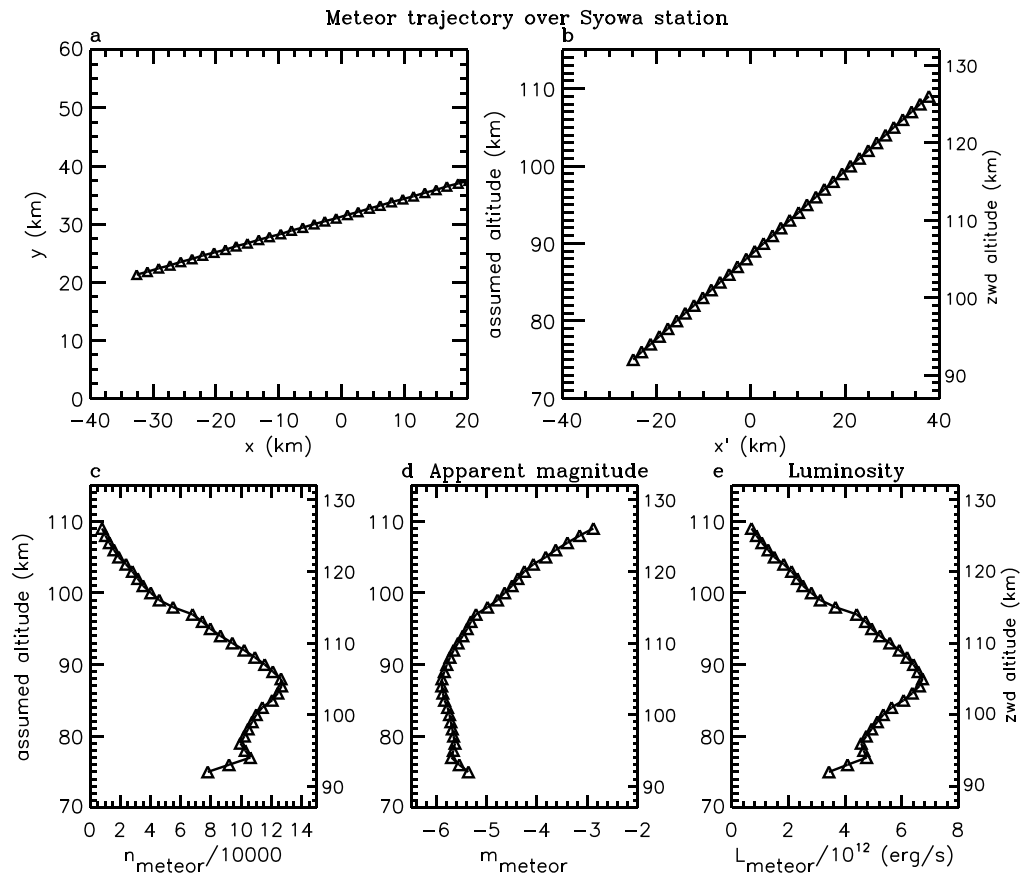


Figure 1. (a) Meteor trajectory projected into the horizontal plane. (b) Meteor trajectory as a function of x' and z . (c) Number of meteor counts observed by the ATV, n_{meteor} (divided by 10^4). (d) Apparent magnitude of the fireball meteor, m_{meteor} . (e) Calculated luminosity of the meteor (divided by 10^{12}). In Figures 1b–1e, the left y axis shows the “assumed altitude,” while the right y axis shows the “zwd altitude.” Here zwd is the deduced altitude assuming that the background winds are zero.

Using the open-source sky simulator program *Stellarium* (available at <http://www.stellarium.org>), the angle ζ_{Jupiter} between Jupiter and the zenith at Syowa Station at the time of the meteor was determined to be 49.84° . The astronomical zenith angle for the meteor is given by $\tan \zeta_{\text{meteor}} = \sqrt{x^2 + y^2}/z$, where $\sqrt{x^2 + y^2}$ is the horizontal distance to the meteor and z is its altitude. Using x , y , and z from Figure 1, we found that ζ_{meteor} varied between 18.4 and 27.4° .

Atmospheric dimming is described via the relation [Chromey, 2010]

$$I = I_0 e^{-kX}. \quad (2)$$

Here I is the intensity ($\text{erg s}^{-1} \text{cm}^{-2}$) observed on the ground, I_0 is the intensity at the top of the atmosphere, and X is the “air mass” (i.e., the ratio of the path length through the atmosphere along the line of sight to the object to the vertical height of the atmosphere looking along the zenith). The dimensionless extinction coefficient k is given by

$$k = \int_0^{z_{\text{top}}} \kappa(z) dz, \quad (3)$$

where z is altitude, $z = z_{\text{top}}$ is the top of the atmosphere, and κ (cm^{-1}) is the absorption coefficient. The value of k for a given location is wavelength-dependent and varies from night to night and often over the course of a single night. For the standard astronomical V or “visual” photometric filter passband, typical values range from about 0.15 to 0.30 [Birney et al., 2006]. Because the upper atmosphere is very tenuous and aerosols (other than those from volcanic eruptions and forest fires) are concentrated toward the surface

[Chromey, 2010], the bulk of the dimming occurs well below the minimum altitude $z = 75$ km of the meteor, so we can neglect the correction for the fact that we do not see the meteor through the entire length of the atmosphere.

Approximating the Earth's surface and the top of the atmosphere as parallel horizontal planes, from simple trigonometry the air mass X is simply $X = \sec \zeta$; curvature effects become significant only for $\zeta > 60^\circ$ ($X = 2$). Using this, the apparent dimming of Jupiter relative to the meteor due to Jupiter's larger air mass is $e^{-k(X_{\text{Jupiter}} - X_{\text{meteor}})}$. Using the maximum difference $X_{\text{Jupiter}} - X_{\text{meteor}} = 0.424$ and $k = 0.15$ gives a dimming of about 6.2%, while $k = 0.30$ yields about 12%. Vignetting would exacerbate this effect. Therefore, we instead looked for another bright object in the images whose zenith angle was closer to that of the meteor.

Fortunately, the zenith angle of the third brightest star in the night sky, α Centauri, was 20.46° at the time of the meteor, nearly the same as that of the meteor, substantially mitigating the effects of both differential dimming and vignetting. Using the maximum difference $X_{\text{meteor}} - X_{\alpha\text{Cen}} = 0.0594$ and $k = 0.15$ gives a dimming of the meteor relative to α Centauri of only $\sim 0.9\%$, while $k = 0.30$ yields about 1.8%. We thus use α Centauri as the comparison star, despite its substantially smaller mean number of counts as compared to Jupiter: $n_{\alpha\text{Cen}} = 727$.

The α Centauri is a double star whose small angular separation is below the resolving power of the TV camera, causing the pair to be imaged as a single point of light. The apparent visual (V -filter) magnitude of the combined pair is -0.285 [Cousins, 1971], while the distance to the system is $d_{\alpha\text{Cen}} = 1.339$ pc [Söderhjelm, 1999]. To obtain the luminosity of the system, we compare its absolute visual magnitude, $M_{V,\alpha\text{Cen}}$, to the absolute visual magnitude of the Sun, $M_{V,\text{Sun}} = 4.83$ [Chromey, 2010]. The relation between the apparent magnitude m , the absolute magnitude M , and the distance d in parsecs is $m - M = 5 \log_{10} d - 5$ [Chromey, 2010], which yields $M_{V,\alpha\text{Cen}} = 4.08$.

The ratio of luminosities through the V -filter passband is then $L_{\alpha\text{Cen}}/L_{\text{Sun}} = 10^{-0.4(M_{V,\text{Sun}} - M_{V,\alpha\text{Cen}})} = 1.99$ [Carroll and Ostlie, 2006]. Because both components of α Centauri are similar in surface temperature to the Sun [Liseau et al., 2013], it is a good approximation that the ratio of their V -filter luminosities is the same as the ratio of their total luminosities. Given the solar luminosity $L_{\text{Sun}} = 3.838 \times 10^{33}$ erg s^{-1} , we obtain $L_{\alpha\text{Cen}} = 7.65 \times 10^{33}$ erg s^{-1} . Then from the distance to α Centauri, $d_{\alpha\text{Cen}} = 1.339$ pc = 4.130×10^{18} cm, the intensity of α Centauri at Earth above the atmosphere is $I_{\alpha\text{Cen}} = L_{\alpha\text{Cen}}/4\pi d_{\alpha\text{Cen}}^2 = 3.57 \times 10^{-5}$ erg s^{-1} cm^{-2} .

Because the amount of atmospheric dimming and vignetting is very similar for the meteor and α Centauri, we obtain the calibrated intensity of the meteor as seen at the ATV camera:

$$I_{\text{meteor}} = \left(\frac{n_{\text{meteor}}}{n_{\alpha\text{Cen}}} \right) I_{\alpha\text{Cen}}. \quad (4)$$

Assuming the meteor radiates isotropically, its luminosity is then

$$L_{\text{meteor}} = 4\pi d_{\text{meteor}}^2 I_{\text{meteor}}, \quad (5)$$

where $d = \sqrt{x^2 + y^2 + z^2}$ is the distance to the meteor.

We compute the apparent magnitude of the meteor via [Chromey, 2010]

$$m_{\text{meteor}} - m_{\alpha\text{Cen}} = -2.5 \log_{10} \left(\frac{I_{\text{meteor}}}{I_{\alpha\text{Cen}}} \right). \quad (6)$$

Figure 1d shows the apparent magnitude of the meteor from equation (6). Because it is brighter than $m_{\text{meteor}} = -4$, this meteor is classified as a "fireball meteor." Note that Venus, the third brightest astronomical object normally visible after the Sun and Moon, is approximately magnitude -4 , so the meteor would be easily visible with the naked eye.

Figure 1e shows the absolute luminosity of the meteor. L_{meteor} is seen to peak at $z \sim 88$ km, which is slightly below the peak in the Na airglow layer (the Na layer peaks at $z = 92$ km; see section 2.3).

As mentioned previously, the meteor's luminosity is composed of light that is created as the meteor "burns up" upon entering the Earth's atmosphere. The meteor's luminosity profile reflects the mass loss or ablation of the meteoric surface, as well as heating of the air around the meteor from the shock wave [Cepplecha et al., 1998]. A cylindrical blast wave forms around a meteor with a radius determined by the meteoroid Mach number and its size (see section 5). Such an atmospheric heating can excite GWs and AWs [Vadas, 2013].

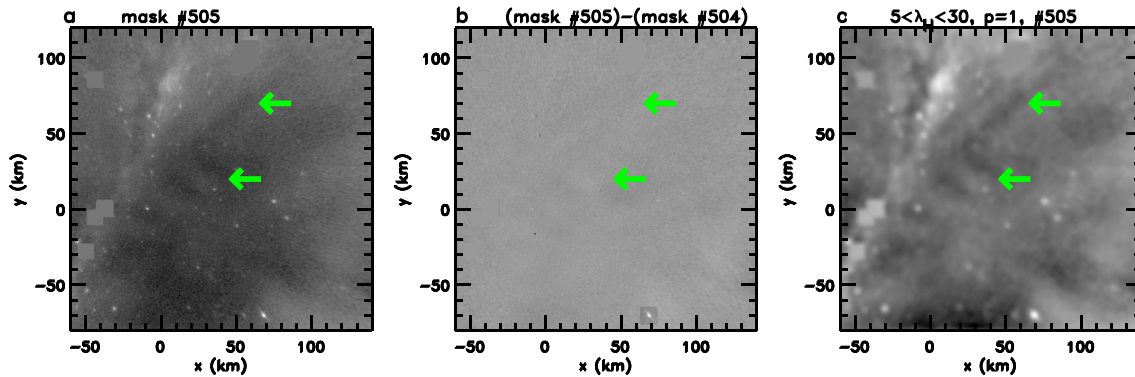


Figure 2. Na airglow images. (a) Mask only for frame #505. (b) Masked image for frame #505 minus the masked image for frame #504. (c) Masked and spectrally filtered image for frame #505. Here we use $\lambda_{\min} = 5$ km, $\lambda_{\max} = 30$ km, and $p = 1$. For all Na airglow images in this paper, maximum positive values are white and maximum negative values are black. The lower green arrows show the location of the southwestward moving waves with phase lines oriented northwest to southeast. The upper green arrows show the northwestward moving waves with phase lines oriented southwest to northeast. Note the distinct V-shaped structures in Figure 2c at $x = [0, 50]$ km and $y = [0, 60]$ km. The open ends of these V-shaped structures point toward the northeast.

2.3. Spectral Filtering of the Na Airglow Images

The ASI (All-Sky Imager for airglow) is a sensitive camera equipped with a cooled CCD sensor, a fish-eye lens ($f = 8$ mm, $F\# = 2.8$), a relay lens, and a band-pass interference filter with a peak transmittance of 64% at 589.3 nm and a band width of 2.7 nm at full width at half-maximum [Taguchi *et al.*, 2004]. This filter is designed to observe the Na emission D-lines from an airglow layer centered at 90 km altitude [e.g., Greer and Best, 1967]. This layer has a typical thickness (full width at half maximum) of ~ 410 km. This instrument operated with a 1 min exposure time every minute during the night.

On 7 June 2008, the ASI took data every minute from the time the meteor was observed for at least an hour afterward. The meteor was observed only in frame #496. Because the aurora was active this night, our Na images are “contaminated” with the aurora. However, this contamination does not prevent the observation of the “fishbone” waves that were seen that night.

We first project (flat-field) each Na image to $z = 92$ km. We then trim each image to 1000×1000 pixels, which corresponds to 400 km \times 400 km in the zonal (x) and meridional (y) directions. Note that the pixel resolution is 0.4 km. In order to eliminate the lower-resolution edges and to enhance the region with the waves, we select a 200 km \times 200 km region centered slightly northeast of the center at pixel # (600, 550).

Because the aurora moves rapidly from one image to the next, auroral “contamination” cannot be removed by time differencing the images in the usual manner [e.g., Yue *et al.*, 2009]. Instead, we mask and Fourier filter each image separately in order to remove as much contamination from planets, stars, and the aurora as possible. First, we calculate the average intensity of each 200 km \times 200 km image, \bar{l} . Then, we locate those pixels (i, j) that have an intensity, l , of $l \geq 2\bar{l}$. For these pixels, we center a square mask of 24×24 pixels at (i, j) and set the intensities of all pixels within that mask equal to \bar{l} . (In frame #496, we utilize a mask that is only 2×2 pixels in the vicinity of the meteor trail in order to prevent masking this trail.) We further isolate the waves by decreasing the effect of a bright background when plotting the images via

$$A = (l - \min(l))^a, \quad (7)$$

where A is the “enhanced relative intensity,” $a = \frac{2}{3}$, and $\min(l)$ denotes the minimum of l . The enhanced relative intensity A is plotted in all of the images in Figures 2–6. Note that when the images are Fourier filtered (see below), the enhanced relative intensity is calculated after this filtering. For all of the images shown in this paper, maximum positive values are white, while maximum negative values are black. Figure 2a shows the masked image at frame #505 or $\Delta t = 9$ min, where Δt is the time elapsed after the meteor was observed. The whitish band from $(x, y) \sim (-60, -40)$ km to $\sim (20, 120)$ km is the Milky Way. Several stars in the Milky Way are masked out. Jupiter is the brightest object in the image and is masked out at $(x, y) \sim (50, 100)$ km. A faint southwestward moving wave train with a horizontal wavelength of $\lambda_H \sim 20$ – 30 km is barely visible to the left of the lower green arrow. These waves have linear phase lines oriented from the meteor trajectory toward the southeast. The phase lines appear to end abruptly at the horizontal projection of the meteor trajectory (for example, at $x = 10$ km, $y = 35$ km). North of the meteor trajectory, very faint waves are seen

moving northwestward (upper green arrow), with phase lines that end abruptly at the horizontal projection of the meteor trajectory. These latter phase lines are oriented from the trajectory toward the northeast. For illustration purposes, Figure 2b shows the difference image: the masked image at frame #505 minus the masked image at frame #504. We see that the aurora dominates this difference image, obscuring the waves.

In order to isolate the waves to a higher degree, we spectrally filter the images. We take a 2-D Fourier transform of each masked image I :

$$I(x, y) = \frac{1}{(2\pi)^3} \int_{-\infty}^{\infty} \int_{-\infty}^{\infty} e^{-i(kx+ly)} \tilde{I}(k, l) dk dl, \quad (8)$$

where “ $\tilde{}$ ” denotes the Fourier transform and k and l are the zonal and meridional wave numbers, respectively. We then filter by horizontal wavelength, $\lambda_H = 2\pi/k_H$, where $k_H = \sqrt{k^2 + l^2}$ is the horizontal wave number of the wave. In order to avoid the introduction of artificial waves at sharp boundaries (such as occurs with a top hat filter), we use the following smoothly varying filter with $p \geq 0$:

$$\tilde{I}_{\text{filter}} = \tilde{I} \begin{cases} (\lambda_H/\lambda_{\min})^p & \text{for } \lambda_H \leq \lambda_{\min} \\ 1 & \text{for } \lambda_{\min} \leq \lambda_H \leq \lambda_{\max} \\ (\lambda_{\max}/\lambda_H)^p & \text{for } \lambda_H \geq \lambda_{\max} \end{cases}. \quad (9)$$

Here λ_{\min} and λ_{\max} are the minimum and maximum wavelengths. We then take the inverse 2-D Fourier transform of $\tilde{I}_{\text{filter}}(k, l)$ to obtain $I_{\text{filter}}(x, y)$. A is then calculated using I_{filter} in place of I in equation (7).

Since the waves we wish to isolate have $\lambda_H \sim 15\text{--}30$ km, we varied λ_{\min} from 0.1 to 10 km. We found that the images are too noisy at small scales for $\lambda_{\min} = 0.1$ km and are too smooth for $\lambda_{\min} = 10$ km (although there is less contamination from stars in this case). The best choice is found to be $\lambda_{\min} = 5$ km. We then varied λ_{\max} from 30 to 80 km. We found that the aurora (and other large-scale background noise features) are too prominent for $\lambda_{\max} = 80$ km, thereby partially obscuring the waves. The best choice is found to be $\lambda_{\max} = 30$ km. We also varied p from 0.5 to 2. We found that $p = 1$ allows the waves to be seen the most clearly. We show the resulting masked, filtered, and enhanced image in Figure 2c. The waves are now much easier to see, although they are still faint. Note that the Milky Way is also visible in this image.

For the rest of the Na images shown in this paper, we Fourier filter the masked images with $\lambda_{\min} = 5$ km, $\lambda_{\max} = 30$ km, and $p = 1$.

3. Na Airglow Observations of the Waves Excited by the Meteor

Sodium (Na) is one of the many constituents of a meteor. As a meteor burns up within the Earth's atmosphere, it is heated via collisions within the atmosphere. Material is ablated from the meteor surface, and light is generated by the deexcitation of excited atoms through discrete spectral lines mainly associated with meteoric metals [Ceplecha et al., 1998]. Photons from the excited sodium within the hot meteor train were detected by the Na airglow imager [Suzuki et al., 2013].

Figure 3a shows frame #496. The meteor is visible at $(x, y) \sim (-40, 30)$ km to $(10, 35)$ km. However, because the Na emission photons might be coming from anywhere along the meteor trajectory (i.e., from $z = 75$ to 110 km from Figure 1), the projection to 92 km causes the meteor's location to be somewhat inaccurate in this Na image, especially for altitudes z that are far from 92 km. Therefore, we overplot the actual meteor trajectory using the ATV camera data (from Figure 1a) as a blue dotted line in Figure 3a. As mentioned in section 2.1, the meteor moved in the direction $180 + \theta_{\text{meteor}} = 197.1^\circ$ counterclockwise from east.

Eight minutes after the meteor passed (i.e., in frame #504), persistent faint waves appeared in more than 18 frames. These waves were visible for ~ 44 min and were not visible after frame #540. In Figures 3b–3i, we highlight eight of these frames. Green arrows show the locations of the waves. These waves have linear phase fronts that appear to originate along the horizontal projection of the meteor trajectory to $z = 92$ km (i.e., along the blue dotted line). This is explicitly seen in frame #505. In the other frames where there is more auroral contamination, we see that the wave phase lines do not extend linearly across the meteor trajectory. A movie of the images show that the waves north of the meteor trajectory move northwestward (frames #505, 538, and 539 in Figure 3), while the waves south of the meteor trajectory move southwestward (frames #505, 508, 509, 511, 525, and 526 in Figure 3). This movie is provided as supporting information. Note that the waves north of the meteor trajectory have smaller λ_H than those south of the trajectory. Additionally,

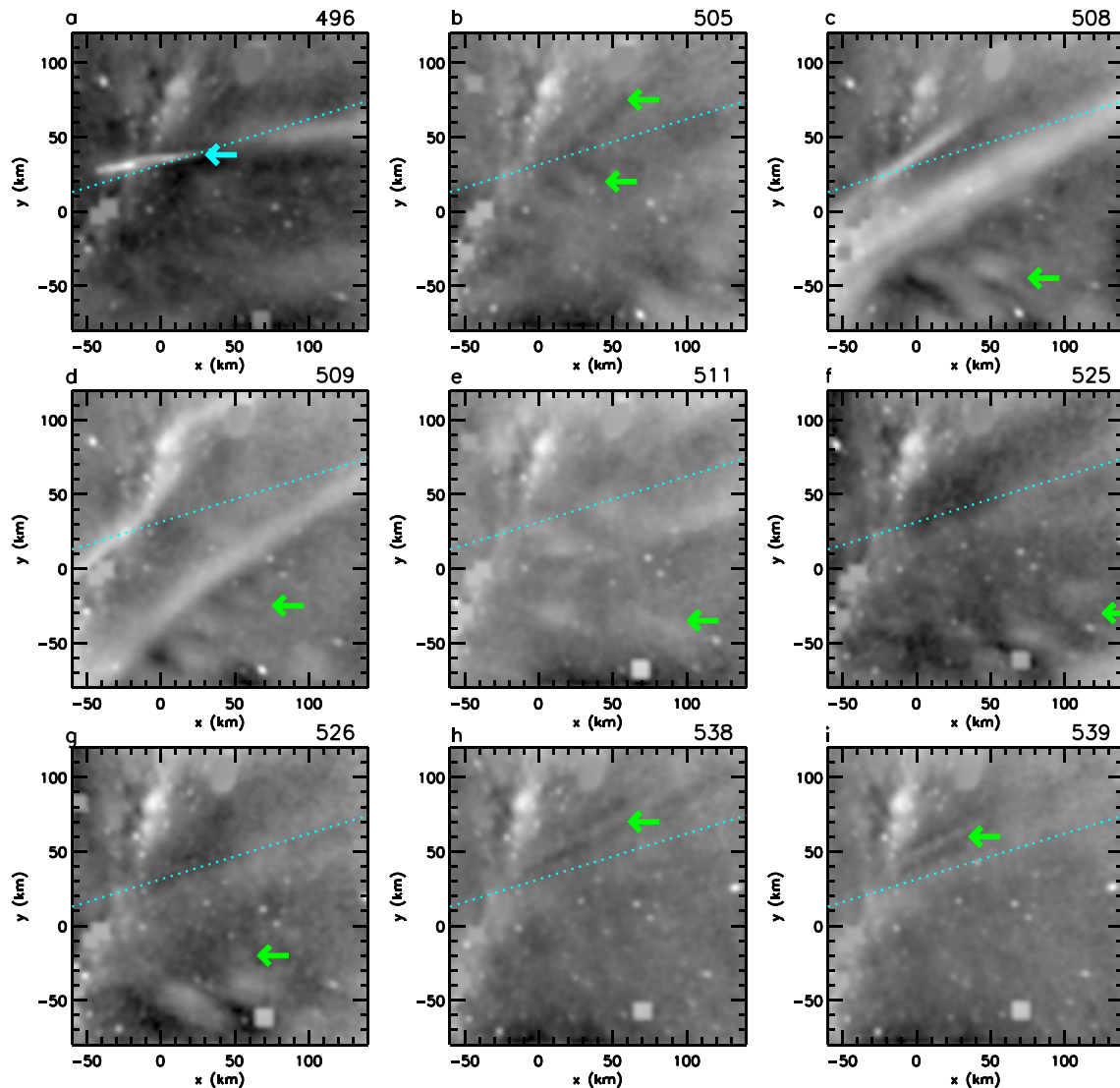


Figure 3. (a–i) Masked and filtered Na airglow images for frames #496, 505, 508, 509, 511, 525, 526, 538, and 539. The blue dotted lines show the horizontal projection of the meteor trajectory as seen by the ATV camera. The blue arrow in Figure 3a shows the northeastern edge of the meteor trail. The green arrows in Figures 3b–3i show the waves. Note the distinct V-shaped structures in frame #505.

the angle of propagation relative to the meteor trajectory is different for those waves north and south of the trajectory.

Figure 4 shows frames #504–512 at “earlier” times, which we define as occurring 8 to 16 min after the fireball meteor. Frame #504 shows the first visible frame where these waves are observed. The blue dotted line shows the meteor trajectory (from Figure 1a). The blue triangle shows the assumed location of the meteor as it passes through the Na airglow layer (i.e., at $z \sim 92$ km). A northwestward moving wave train is seen in frames #505–506 north of the meteor trajectory, while a southwestward moving wave train is seen in frames #505–511 south of the meteor trajectory. Figure 5 shows frames #524–539 at “later” times, which we define as occurring 28–43 min after the fireball meteor. A northwestward moving wave train is seen in frames #532–539 north of the path, while a southwestward moving wave train is seen in frames #524–532 south of the meteor trajectory.

In order to determine the phase speeds and horizontal wavelengths of these waves, we visually fit “plane waves” that end abruptly at the meteor trajectory to the observed waves. This fit is done visually because of the auroral contamination in the Na images. The fitted parameters include the horizontal wavelength λ_H , the horizontal phase speed c_H , and the angle θ counterclockwise from east of the constant phase line of the

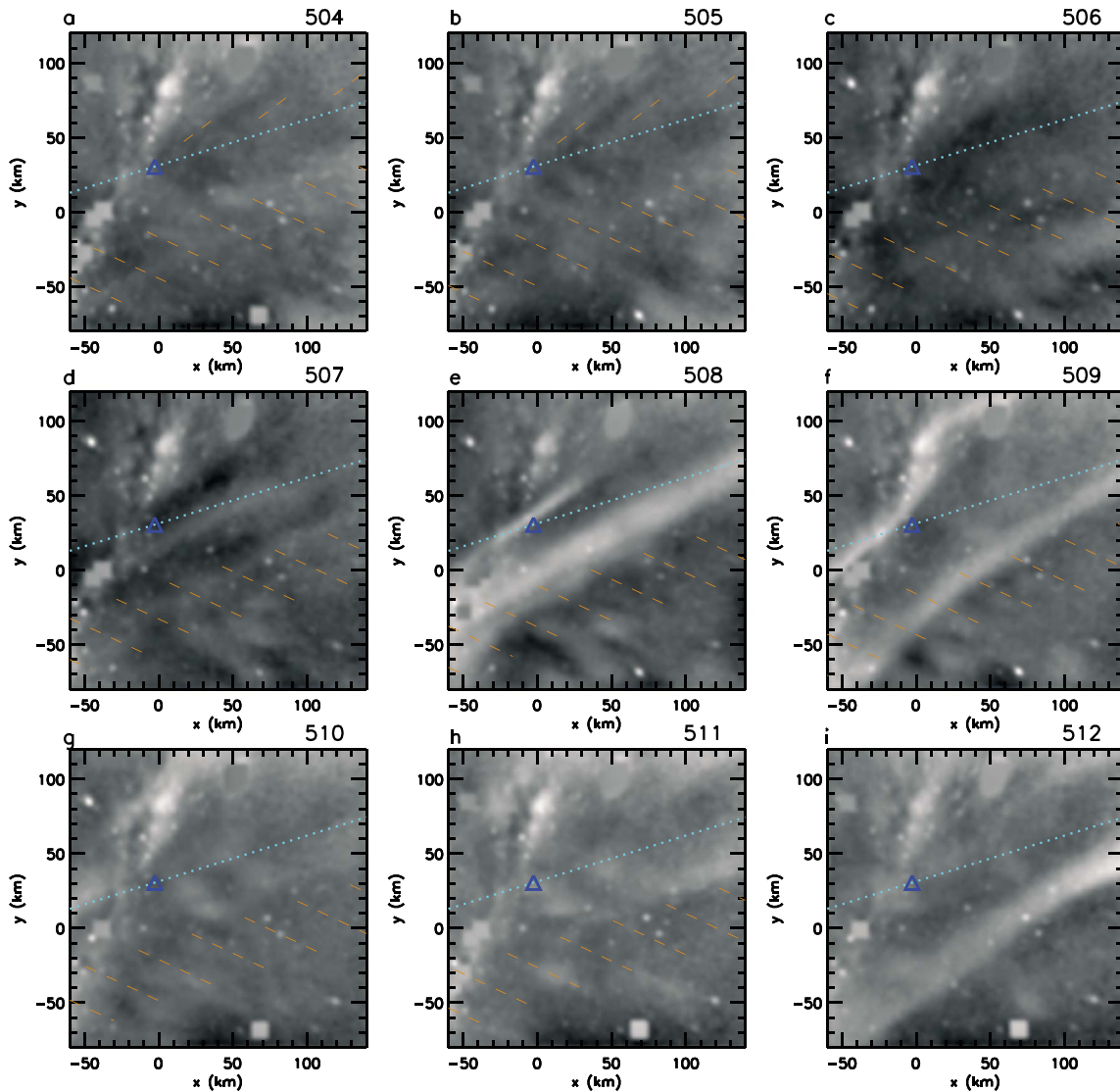


Figure 4. (a–i) Masked and filtered Na airglow images for earlier times (frames #504–512). The blue dotted lines show the meteor trajectory. The blue triangles show the assumed location of the meteor at $z = 92$ km. The orange-brown dashed lines show portions of the best fit plane waves, as described in the text.

wave. The angle between the wave’s constant phase line and the meteor trajectory is then $\theta - \theta_{\text{meteor}}$. We determine the parameters for four distinct wave trains: the northwestward moving wave trains north of the meteor trajectory at early and late times and the southwestward moving wave trains south of the meteor trajectory at early and late times. Early times are defined as frames #504–512, while late times are defined as frames #524–539. The best fit parameters are determined visually and are listed in Table 1. The observed wave periods are calculated via $\tau_r = \lambda_H / c_H$.

In order to see the “goodness” of the fits, we overlay these best fit plane wave trains in Figures 4 and 5 as orange-brown dashed lines. Here we plot only a portion of the phase lines, in order to better see the small-amplitude (and often faint) modulations of the waves. These lines are not shown if the wave phase lines are quite faint. We first examine the waves north of the meteor trajectory. At early times, this wave train has $\lambda_H = 18$ km, $c_H = 20$ m/s, an observed period of $\tau_r = 15$ min, and a phase line angle of $\theta = 37^\circ$ from Table 1. From Figure 4, we see that the best fit plane waves fit this northwestward moving wave train well, although there are only two images from which to determine the wave parameters. At late times, the wave train has $\lambda_H = 18$ km, $c_H = 40$ m/s, $\tau_r = 7.5$ min, and $\theta = 27.5^\circ$. From Figure 5, we see that the best fit plane wave fits this northwestward moving wave train well. For this wave train, the GW phase lines are nearly parallel to the meteor trajectory.

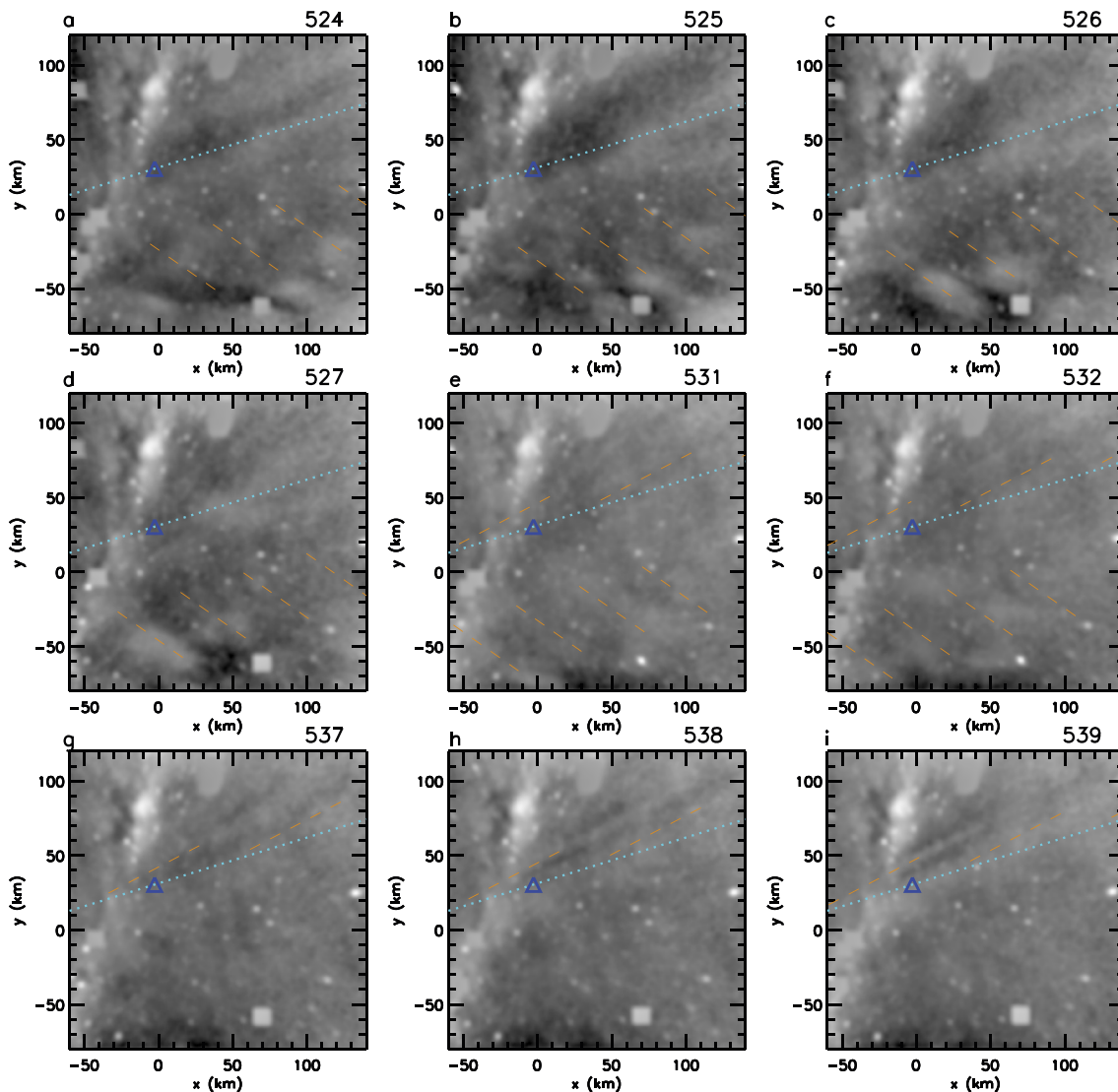


Figure 5. Same as in Figure 4 but for later times (frames #524–539).

We now examine the waves south of the meteor trajectory. At early times, this wave train has $\lambda_H = 25$ km, $c_H = 80$ m/s, $\tau_r = 5.2$ min, and $\theta = -25^\circ$. At late times, this wave train has $\lambda_H = 35$ km, $c_H = 100$ m/s, $\tau_r = 5.8$ min, and $\theta = -35^\circ$. Both best fit plane waves fit the southwestward moving waves well in Figures 4 and 5.

Because these waves propagate in directions perpendicular to their phase fronts (see also the movie mentioned above), have periods greater than the buoyancy period (~ 5 min), and have phase speeds less than the sound speed (~ 300 m/s), these waves are likely atmospheric gravity waves (GWs). In the next section, we calculate the GWs and acoustic waves (AWs) excited by idealized line-shaped heat/forcings and compare with these observations.

In addition to these waves, very faint waves are also apparent in the western portion of the Na airglow images for frames #525 and 526. Figure 6 shows the western portion of the Na images for frames #505, 525, and 526. The green arrow in Figure 6a shows the location of the southwestward moving GWs from Figure 4b (diagnosed previously). In Figures 6b and 6c, very faint GWs can be seen with phase lines that are aligned toward the northwest and southwest from the meteor trajectory, as indicated by the upper (northern) and lower (southern) pink arrows, respectively. These phase lines appear to end along the horizontal projection of the meteor trajectory. The waves north of the meteor trajectory (upper pink arrows)

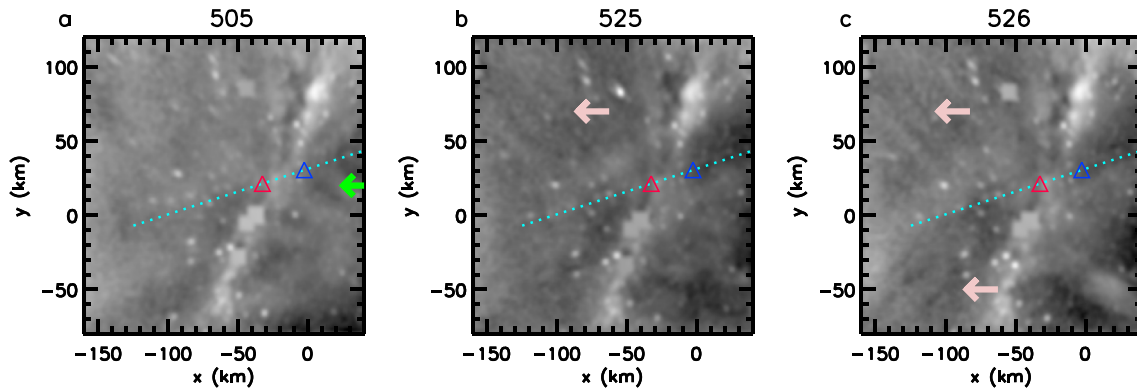


Figure 6. (a–c) Western portions of the masked and filtered Na airglow images for frames #505, 525, and 526. The green arrow in Figure 6a indicates the V-shaped waves at $x \sim 20$ km and $y \sim 20$ km identified in Figures 3b and 4b. The upper (lower) light pink arrows in Figures 6b and 6c denote faint northeastward (southeastward) moving V-shaped waves likely excited by the meteor. The blue triangles show the assumed location of the meteor at $z = 92$ km. The red triangles show the observed (estimated) location of the “X,” as described in the text.

propagate northeastward, while the waves south of the meteor trajectory (lower pink arrow) propagate southeastward. These waves are much fainter than the waves previously diagnosed in the eastern portion of the Na airglow images (e.g., Figure 3). We mark the approximate center of the X structure (formed by the oppositely-directed Vs) with a red triangle. We note that there is uncertainty associated with the identification of these weaker GWs and of the location of the X.

Although the waves shown in Figures 4–6 were first noticeable ~ 5 min after the meteor passage and have phase lines which appear to originate along the horizontal projection of the meteor trajectory, it is possible that they are merely coincidental and are not at all connected with the meteor. However, this seems unlikely for several reasons. First, it is well known that meteor ablation heats the atmosphere. Any atmospheric heating with a duration less than an hour generates high-frequency GWs [Vadas and Fritts, 2001; Vadas, 2013]; thus, GWs are expected to be generated by this event. Second, there are very few processes which can create GW phase lines that end sharply at an “invisible” edge when no man-made boundary or natural interface (e.g., air/water) is present. It turns out that slanted heat/forcings are among these processes (see section 4). (Typical GW excitation processes create GWs with phase line edges that look “frayed” and evolve in time.) We therefore proceed in section 4 with modeling slanted, line-shaped heatings and body forcings in the MLT. This is important in order to estimate the heating parameters necessary to generate the observed waves. We will then argue why several of these parameters make sense in section 5.

4. Modeling the GWs and AWs Excited by a Fireball Meteor

In this section, we model the GWs and AWs excited by horizontal and slanted heatings and a three-dimensional (3-D) slanted body force in the mesosphere and lower thermosphere (MLT). We consider a local, interval heating and/or 3-D body force in an inviscid neutral fluid. Each heat/forcing turns on and off smoothly over a finite interval in time. The compressible momentum, mass, and energy conservation equations are

$$\frac{D\mathbf{v}}{Dt} + \frac{1}{\rho} \nabla p - \mathbf{g} + 2\boldsymbol{\Omega} \times \mathbf{v} = \mathbf{F}(\mathbf{x})\mathcal{F}(t) \quad (10)$$

$$\frac{D\rho}{Dt} + \rho \nabla \cdot \mathbf{v} = 0 \quad (11)$$

Table 1. “Best Fit” GW Parameters From the Na Airglow Images

Wave Location	λ_H (km)	c_H (m/s)	τ_r (min)	θ (deg)	$\theta - \theta_{\text{meteor}}$ (deg)
North of meteor trajectory, early times	18	20	15	37	19.9
North of meteor trajectory, late times	18	40	7.5	27.5	10.4
South of meteor trajectory, early times	25	80	5.2	−25	−42.1
South of meteor trajectory, late times	35	100	5.8	−35	−52.1

$$\frac{DT}{Dt} + (\gamma - 1)T\nabla \cdot \mathbf{v} = J(\mathbf{x})\mathcal{F}(t), \quad (12)$$

where $D/Dt = \partial/\partial t + (\mathbf{v} \cdot \nabla)$, $\mathbf{v} = (u, v, w)$ is the velocity vector, u , v , and w are the zonal, meridional, and vertical velocities, respectively, T is the temperature, ρ is the density, p is the pressure, $\boldsymbol{\Omega}$ is the Earth's rotation vector, \mathbf{g} is the Earth's gravitational force, $p = r\rho T$ is the ideal gas law, $\mathbf{F}(\mathbf{x})\mathcal{F}(t)$ is the 3-D body force, $J(\mathbf{x})\mathcal{F}(t)$ is the heating/cooling, $r = 8308/X_{\text{MW}} \text{ m}^2 \text{ s}^{-2} \text{ K}^{-1}$, X_{MW} is the mean molecular weight of the particle in the gas, $\gamma - 1 = r/C_v$, and C_v is the mean specific heat at constant volume. Using the ideal gas law, equation (12) can be rewritten in terms of the pressure:

$$\frac{Dp}{Dt} + \gamma p \nabla \cdot \mathbf{v} = \frac{p}{T} J(\mathbf{x})\mathcal{F}(t). \quad (13)$$

The spatial portion of the 3-D body force is $\mathbf{F}(\mathbf{x}) = F_x(\mathbf{x})\hat{i} + F_y(\mathbf{x})\hat{j} + F_z(\mathbf{x})\hat{k}$, where \hat{i} , \hat{j} and \hat{k} are the zonal, meridional, and vertical unit vectors, respectively. The spatial portion of the heating is $J(\mathbf{x})$. Positive (negative) F_x and F_y denote an eastward (westward) and a northward (southward) forcing, respectively. Positive (negative) F_z denotes an upward (downward) forcing. Positive (negative) J denotes a heating (cooling). The functions F_x , F_y , F_z , and J can be any arbitrary functions of (x, y, z) , although they and their spatial derivatives must be continuous. We choose a smoothly varying time dependence for the heatings and body forces:

$$\mathcal{F}(t) = \frac{1}{\chi} \begin{cases} (1 - \cos[\hat{a}(t - t_0)]) & \text{for } t_0 \leq t \leq t_0 + \chi \\ 0 & \text{for } t \leq t_0 \text{ and } t \geq t_0 + \chi. \end{cases} \quad (14)$$

Here χ is the total duration of the force/heating, n is the number of cycles, $\hat{a} = 2\pi n/\chi$ is the heat/forcing frequency, and t_0 is the initial time that the heat/forcing begins. We set $n = 1$ for all model results shown in this paper.

We expand the variables as background means (overlines) plus perturbations (primes):

$$\begin{aligned} u &= \bar{u} + u', & v &= \bar{v} + v', & w &= w', \\ \rho &= \bar{\rho} + \rho', & T &= \bar{T} + T', & p &= \bar{p} + p'. \end{aligned} \quad (15)$$

We neglect the Earth's curvature, which limits wave scales to $\lambda_H < 20,000\text{--}30,000$ km. We also neglect the Coriolis force (i.e., set $f = 0$), because it is ineffective for wave periods less than a few hours. Linearizing equations (10)–(11) and (13), we obtain

$$\frac{\partial \mathbf{v}'}{\partial t'} + \frac{1}{\bar{\rho}} \nabla \rho' - \frac{\rho'}{\bar{\rho}^2} \nabla \bar{p} + f(-v'\hat{i} + u'\hat{j}) = \mathbf{F}(\mathbf{x})\mathcal{F}(t), \quad (16)$$

$$\frac{\partial \rho'}{\partial t'} + (\mathbf{v}' \cdot \nabla) \bar{\rho} + \bar{\rho} \nabla \cdot \mathbf{v}' = 0, \quad (17)$$

$$\frac{\partial p'}{\partial t'} + \mathbf{v}' \cdot \nabla \bar{p} + \gamma \bar{p} \nabla \cdot \mathbf{v}' = \frac{\bar{p}}{T} J(\mathbf{x})\mathcal{F}(t), \quad (18)$$

where $\partial/\partial t' = (\partial/\partial t) + \bar{u}\partial/\partial x + \bar{v}\partial/\partial y$. The solutions to equations (16)–(18) were derived in Vadas [2013] for an isothermal temperature profile. These solutions take into account the exponential decay in altitude of the neutral background density. Therein, it was shown that heat/coolings and body forces always excite GWs and AWs. The amplitudes of these waves are linearly proportional to the heat/forcing amplitude. Because a heating/cooling/forcing creates an unbalanced fluid, and because such a fluid reacts to rebalance itself via the generation of GWs and AWs, any amplitude for the heat/forcing will result in the excitation of GWs and AWs (i.e., there is no minimum amplitude below which GWs and AWs are not created) [Vadas, 2013]. Additionally, the horizontal and vertical scales of these excited GWs and AWs are independent of the heat/force amplitude. Instead, these scales depend on the horizontal/vertical scales of the heat/force and on its duration. For simple heat/forcings with durations much less than the buoyancy period, the scales of the excited GWs only depend on the length and width of the heat/forcing, not on its duration [Vadas and Fritts, 2001; Vadas et al., 2003]. This is partially the case here, since the heat/force duration is ~ 5 min (see below), which is of the order of the buoyancy period.

Our purpose here is not only to model the heat/forcing which produces results similar to those seen in the Na airglow observations but also to understand more generally the characteristics of the GWs excited by heat/forcings with various lengths and widths and at a variety of altitudes within MLT. However, we confine

our results to relatively short-duration heat/forcings of 5 min. Although the meteor moved rapidly and was only visible in the MLT for ~ 70 km/(69 km/s) ~ 1 s (see Figure 1b), shock heating and diffusion processes were likely of the order of ~ 5 min (see section 5). Therefore, we choose a heat/force duration of $\chi = 5$ min. Additionally, we assume a background temperature of $\bar{T} = 205$ K, which was the measured temperature in the OH airglow layer at $z \sim 86$ km [Suzuki *et al.*, 2010]. We set the mean molecular weight X_{MW} and γ to typical MLT values: $X_{MW} = 30$ and $\gamma = 1.4$. The sound speed is $c_s = \sqrt{\gamma r \bar{T}}$, where $r = 8308/X_{MW} \text{ m}^2 \text{ s}^{-2} \text{ K}^{-1}$. For this fluid, $c_s = 282$ m/s and $H = 5.96$ km. The buoyancy frequency is $N_B = \sqrt{(\gamma - 1)g/c_s}$. Here $N_B = 0.0214 \text{ s}^{-1}$, yielding a buoyancy period of $\tau_b = 2\pi/N_B = 4.9$ min.

4.1. GWs and AWs Excited by Line-Shaped Heatings

As a fireball meteor enters the atmosphere and interacts with the molecules via collisions, it will generate a shock wave. This wave, coupled with diffusion, will heat the atmosphere in the region surrounding the meteor (see section 5). In order to understand the basic properties of the GWs and AWs excited by this heating, we model the spatial portion of this line-shaped heating as a Gaussian distribution in space. This idealized heating is slanted in a direction aligned along the meteor's path.

Consider a meteor that travels through the atmosphere with an angle θ counterclockwise from east and with an angle from the horizontal of ψ . In order to model this heating as a Gaussian in space, we first set the coordinate system to be at the center of the heating, i.e., at (x_0, y_0, z_0) :

$$\begin{aligned}\delta x &= x - x_0, \\ \delta y &= y - y_0, \\ \delta z &= z - z_0.\end{aligned}\tag{19}$$

Next, we rotate the coordinate system toward the zenith (around the y axis) by ψ :

$$\begin{aligned}x' &= \delta x \cos \psi - \delta z \sin \psi \\ y' &= \delta y \\ z' &= \delta x \sin \psi + \delta z \cos \psi.\end{aligned}\tag{20}$$

Finally, we rotate the coordinate system in the horizontal plane (around the z axis) by θ :

$$\begin{aligned}x'' &= x' \cos \theta + y' \sin \theta \\ y'' &= -x' \sin \theta + y' \cos \theta \\ z'' &= z'.\end{aligned}\tag{21}$$

We define the spatial portion of this Gaussian heating to be

$$J(x, y, z) = \frac{\gamma H}{r} J_{B0} \exp\left(-\frac{(x'')^2}{2\sigma_{x''}^2} - \frac{(y'')^2}{2\sigma_{y''}^2} - \frac{(z'')^2}{2\sigma_{z''}^2}\right),\tag{22}$$

where J_{B0} is a constant. In this rotated coordinate system, x'' is the coordinate along the meteor's path, and y'' and z'' are the coordinates perpendicular to the meteor's path. The full "parallel" length of this heating is defined as $L_{x''} = 4.5\sigma_{x''}$, and the full "perpendicular" width (i.e., full diameter) of this heating is defined as $L_{y''} = 4.5\sigma_{y''} = 4.5\sigma_{z''}$ [Vadas and Fritts, 2001]. The "4.5" multiplier is convenient, because it was found in Vadas *et al.* [2003] that the most common horizontal length scales of the GWs excited by such a heating is $\sim 2L_{x''}$ and $\sim 2L_{y''}$ if χ is small enough. If the heating is maximum at t_{\max} and has a duration of χ , it begins at $t_0 = t_{\max} - \chi/2$.

Our purpose here is to understand the horizontal scales, phase speeds, and structure of the GWs excited by heatings in the MLT. We will not be taking into account chemistry, nor will we be relating the energy/momentum deposited by the meteor with the amplitudes of the excited GWs, because these tasks are beyond the scope of this paper. Therefore, we choose $J_{B0} = 20 \text{ m/s}^2$ for all heatings shown in this section. This amplitude is arbitrarily chosen and is not related to the meteor ablation process. Integrating equation (12) in time, the maximum value of the right-hand side (at $x'' = y'' = z'' = 0$) is $\gamma H J_{B0}/r \sim 600$ K. Most of this energy goes into mean effects. As we will see in a moment, such slanted heatings lead to temperature perturbations of 1–7% for $z_0 \sim 120$ km.

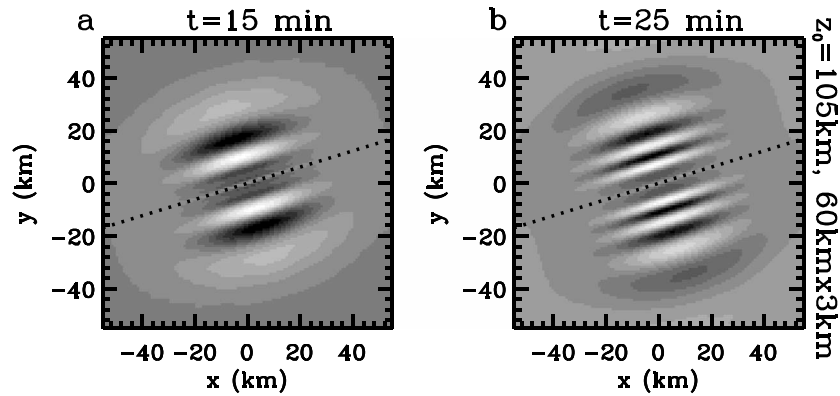


Figure 7. Temperature perturbations at $z = 92$ km associated with the GWs excited by a line-shaped model heating with $z_0 = 105$ km, $L_{x''} = 60$ km, and $L_{y''} = 3$ km. This model heating has $\psi = 0$ and $\theta = \theta_{\text{meteor}}$ and so is “horizontally aligned” with no vertical slant. (a) $t = 15$ min. (b) $t = 25$ min. The maximum values in Figures 7a and 7b are 0.8 and 1.1%, respectively. The black dashed line shows the coordinate x'' . Maximum positive (negative) values are white (black) for all model images in this paper.

4.1.1. GWs Excited by a Horizontally Aligned Line-Shaped Heating in Zero Wind

We first consider a simple line-shaped heating that lies within the horizontal plane above the Na airglow layer: $\theta = \theta_{\text{meteor}} = 17.1^\circ$, $\psi = 0$, $x_0 = y_0 = 0$, and $z_0 = 105$ km. This heating contains no (vertical) slant and might result from a meteor which horizontally skims the surface of the atmosphere. We choose a full length of $L_{x''} = 60$ km and a relatively narrow width of $L_{y''} = 3$ km. Additionally, we choose $x_0 = y_0 = 0$ and a windless background: $U = V = 0$. Upward and downward propagating GWs are created by this heating. Figure 7 shows the resulting temperature perturbations at $z = 92$ km at several times. (These solutions display equations (48)–(49) of Vadas [2013].) The phase lines of the excited GWs are linear and are parallel to the long axis of the heating (i.e., along the x'' direction). At $z = 92$ km, the phase lines of the GWs move away from the heating in a direction perpendicular to x'' . The horizontal wavelength, λ_H , increases with distance from x'' at a given time t . Additionally, λ_H decreases in time as the slower GWs reach the Na layer. Note that a heating below $z = 92$ km yields similar results (not shown).

4.1.2. GWs Excited by Slanted Line-Shaped Heatings in Zero Wind

Next, we consider line-shaped, vertically slanted heatings which lie along the path of the observed meteor. Because we choose the heatings to lie along the meteor trajectory, we calculate its center (x_0, y_0) via

$$\begin{aligned} x_0 &= 27.3 + \cos(\theta_{\text{meteor}}) \frac{(109 - z_0)}{\tan(\psi_{\text{meteor}})} \\ y_0 &= 39.7 + \sin(\theta_{\text{meteor}}) \frac{(109 - z_0)}{\tan(\psi_{\text{meteor}})}, \end{aligned} \quad (23)$$

where the lengths are in kilometers, $\theta_{\text{meteor}} = 17.1^\circ$, and $\psi_{\text{meteor}} = -28.5^\circ$.

Figure 8a shows the results for a heating below the Na layer at $z_0 = 80$ km. Here we choose a short full length of $L_{x''} = 60$ km in order to confine the heating below the Na layer. We also choose a width of $L_{y''} = 10$ km, because as mentioned previously the radiated waves will have horizontal wavelengths of the order $\sim 2L_{y''} \sim 20$ km. We set $U = V = 0$ in order to understand the basic properties of the excited GWs without the complication of Doppler shifting from background winds. GWs are excited with phase lines forming a V-shaped structure. The open end of the V points toward the southwest. The blue triangle shows the central location of the heating at $z = 92$ km, which is also the assumed location of the meteor at $z = 92$ km. These waves occur west of the location where the meteor was at $z = 92$ km. Those waves south of the meteor trajectory move southeastward, while those north of the meteor trajectory move northeastward. The GW phase lines appear to originate along the horizontal projection of the meteor trajectory, although this is not actually what is occurring. The southwestward direction of the open end of the V occurs because the heating slopes downward toward the southwest, below the Na layer. Then, although line-shaped GWs parallel to the heating are created, those that are observed simultaneously at $z = 92$ km come from different altitudes and have different phases. This results in a V-shaped structure at $z = 92$ km. The fact that the GW phase lines are linear (rather than curved) occurs because the length divided by the width of the heating is

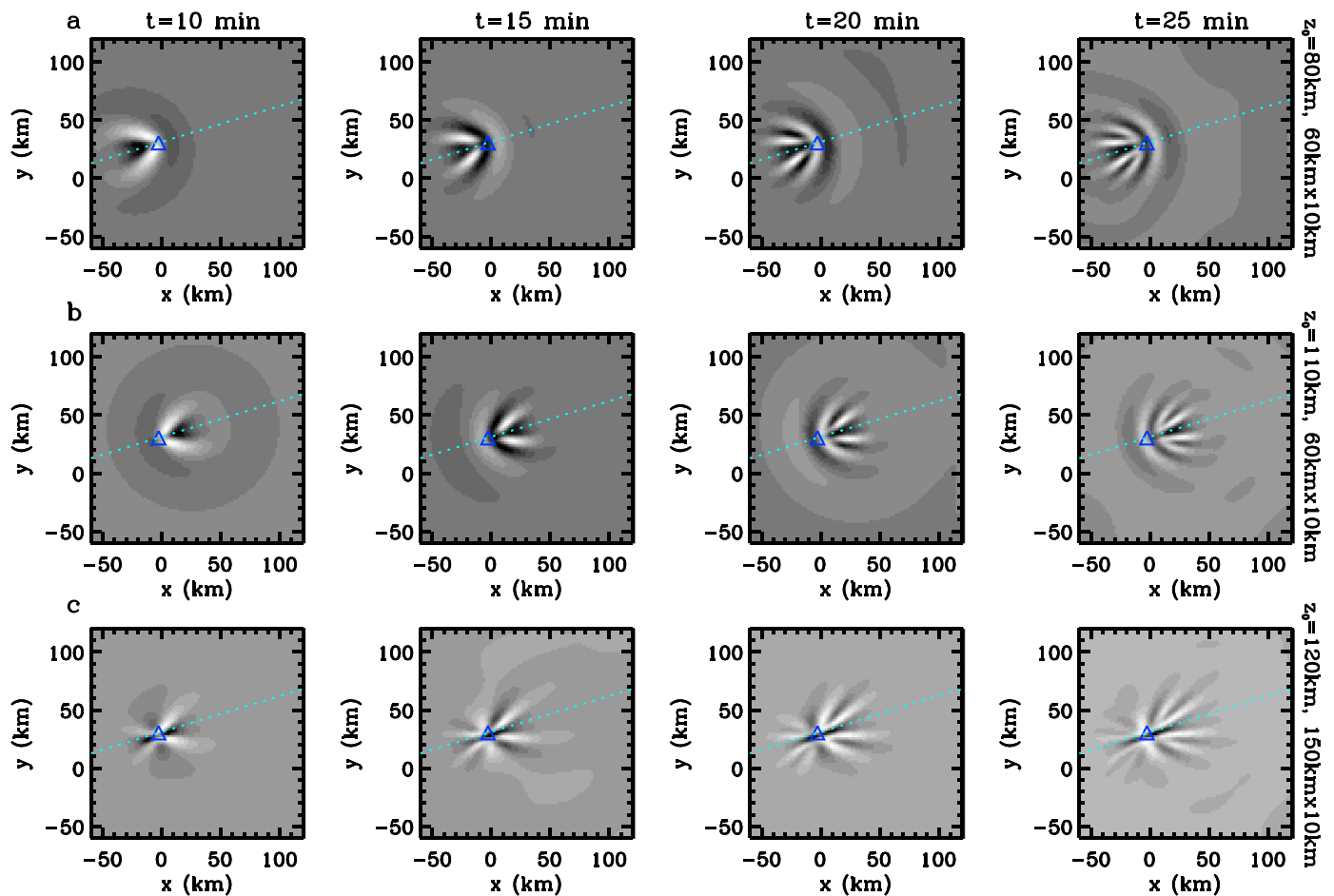


Figure 8. Temperature perturbations at $z = 92$ km associated with the GWs excited by model heatings slanted along the meteor trajectory with $\psi = \psi_{\text{meteor}}$ and $\theta = \theta_{\text{meteor}}$. In each row, we show $t = 10, 15, 20,$ and 25 min from left to right, respectively. (a) $z_0 = 80$ km, $L_x = 60$ km, and $L_y = 10$ km. The maximum values are 42, 48, 41, and 32%, respectively. (b) $z_0 = 110$ km, $L_x = 60$ km, and $L_y = 10$ km. The maximum values are 4, 4, 3, and 3%, respectively. (c) $z_0 = 120$ km, $L_x = 150$ km, and $L_y = 10$ km. The maximum values are 6, 5, 4, and 4%, respectively. The blue dotted lines show the meteor trajectory. The blue triangles show the assumed location of the meteor at $z = 92$ km.

much larger than 1. Indeed, point or spherical sources yield concentric rings of GWs instead [e.g., *Vadas et al., 2009*]. Note that the horizontal wavelengths are smaller at later times: $\lambda_H \sim 10\text{--}15$ km.

Figure 8b shows the results for the same heating as in Figure 8a but centered above the Na layer at $z_0 = 110$ km. This heating also creates GWs with phase lines that form a V-shaped structure. However, here the open end of the V points toward the northeast. As in Figure 8a, these lines appear to originate along the horizontal projection of the meteor trajectory, although as before this is not actually what is occurring. These waves are created at higher altitudes and are therefore downward propagating at $z = 92$ km. Those waves south of the meteor trajectory move southwestward, while those north of the meteor trajectory move northwestward. It is important to note that the direction of the V shape in Figure 8b better reproduces the GW structure in Figures 4 and 5 than the V-shaped structure in Figure 8a.

Figure 8c shows the results for a heating at $z_0 = 120$ km. This heating has the same width of $L_y = 10$ km but has a much longer full length of $L_x = 150$ km. We choose a long full length here in order to examine what happens if most of the heating occurs above the Na layer, but some heating also occurs below it. The result is a “superposition” of Figures 8a and 8b. GWs forming a V-shaped structure with an open end pointing toward the northeast are created east of the blue triangle, and GWs forming a V-shaped structure with an open end pointing toward the southwest are created west of the blue triangle. However, because the amplitude of the heating below the Na layer is smaller than that above it, the GW amplitudes west of the blue triangle are smaller than those east of the blue triangle. Note that the center of the GW structure forms an X where the heating is located at $z = 92$ km (i.e., blue triangle). Figure 8c reproduces many of the

properties of the waves observed in the Na airglow data (i.e., in Figures 4–6). Therefore, we conclude that the center of the slanted heating lies above the Na airglow layer, so that most of the heating occurs above the Na layer. However, we also surmise that the heating must be long enough to cause some heating below the Na layer.

Although the general characteristics of the waves in Figure 8 agree well with the data, we see that the GWs cannot be seen more than ~ 30 km from the meteor trajectory. This is different from the observations, where the GWs are seen up to ~ 70 km from the meteor trajectory (see Figure 3). Increasing the heating width, $L_{y''}$, can lengthen this distance, as we shall see in a moment.

As mentioned above, the X of the GW structure in Figure 8c occurs at the location where the meteor passes through $z = 92$ km. If we assume that the background wind at the excitation altitude is negligible, then the blue triangle in Figures 4 and 5 (which represents the “assumed” location of the meteor at $z = 92$ km) should be colocated with the red triangle in Figure 6 (which shows the location of the X of the GW structure). Because they are not colocated, one possibility is that there was a southwestward background wind at $z = 92$ km which shifted the GW structure southwestward (see section 4.1.3). Another possibility is that our assumed altitude profile for the meteor was too low (see section 2.1). For this latter possibility, we deduce that at $z = 92$ km, the meteor may have been located at $x \sim -33$ km and $y \sim 21$ km (which is the most southwestward location the meteor was observed by the ATV). Because the assumed altitude at this location was 75 km, we might deduce that the meteor was ~ 17 km higher than its estimated altitude (if the background winds are zero):

$$\text{“zwd altitude”} \sim \text{“assumed altitude”} + 17 \text{ km}, \quad (24)$$

where zwd is the zero-wind-deduced altitude. We note that, using the zwd altitude, the meteor’s geocentric velocity was calculated to be 78 ± 1 km/s. This velocity may be too large because the maximum geocentric velocity a meteor can have and remain in a subbound orbit is 72 km/s, unless sling shot by a planet such as Jupiter (D. Janches, personal communication, 2013). It is not possible using our idealized solutions to diagnose which possibility is the most likely. However, because large horizontal background winds are common in the MLT, a shift due to the background wind is the most likely cause for the shift in the X of the GW structure (see section 4.1.3).

Assuming zero background winds for the purpose of modeling, we redefine the center of the heating, (x_0, y_0) , to be consistent with equation (24):

$$\begin{aligned} x_0 &= -32.6 + \cos(\theta_{\text{meteor}}) \frac{(92 - z_0)}{\tan(\psi_{\text{meteor}})} \\ y_0 &= 21.3 + \sin(\theta_{\text{meteor}}) \frac{(92 - z_0)}{\tan(\psi_{\text{meteor}})}, \end{aligned} \quad (25)$$

where the lengths are in kilometers, $\theta_{\text{meteor}} = 17.1^\circ$, and $\psi_{\text{meteor}} = -28.5^\circ$. We emphasize that this redefinition assumes that the background wind is negligible. If a constant southwestward wind were present, the GW structure (and the X) would be shifted toward the southwest in the Na airglow images (see section 4.1.3). Our purpose in redefining the center of our model heating is to colocate it with the X in the observations in order to better compare our model results with the observations.

Figure 9a shows the resulting temperature perturbations T'/\bar{T} at $z = 92$ km for a model heating at $z_0 = 120$ km with $L_{x''} = 150$ km and $L_{y''} = 15$ km. The x_0 and y_0 are determined from equation (25). We set $U = V = 0$ in Figure 9. These results are shown $\Delta t = 10$ to 25 min after the fireball meteor. Southwestward, northwestward, southeastward, and northeastward GWs are created by the heating, although the former two directions (east of the red triangle) have larger amplitudes than the latter two directions (west of the red triangle). Note that the GW phases are linear and appear to originate along the horizontal projection of the meteor trajectory. The horizontal wavelengths are quite a bit larger here. Although they vary, we estimate $\lambda_H \sim 20\text{--}30$ km.

Figure 9b shows the results for the same model heating with lengths and widths of $L_{x''} = 120$ km and $L_{y''} = 10$ km, respectively. The excited GWs have $\lambda_H \sim 30\text{--}40$ km at early times and $\lambda_H \sim 10\text{--}30$ km at later times. The horizontal wavelengths are larger for phase lines which intersect near the red triangle and are smaller for phase lines which intersect further from the red triangle. Note that the southeastward

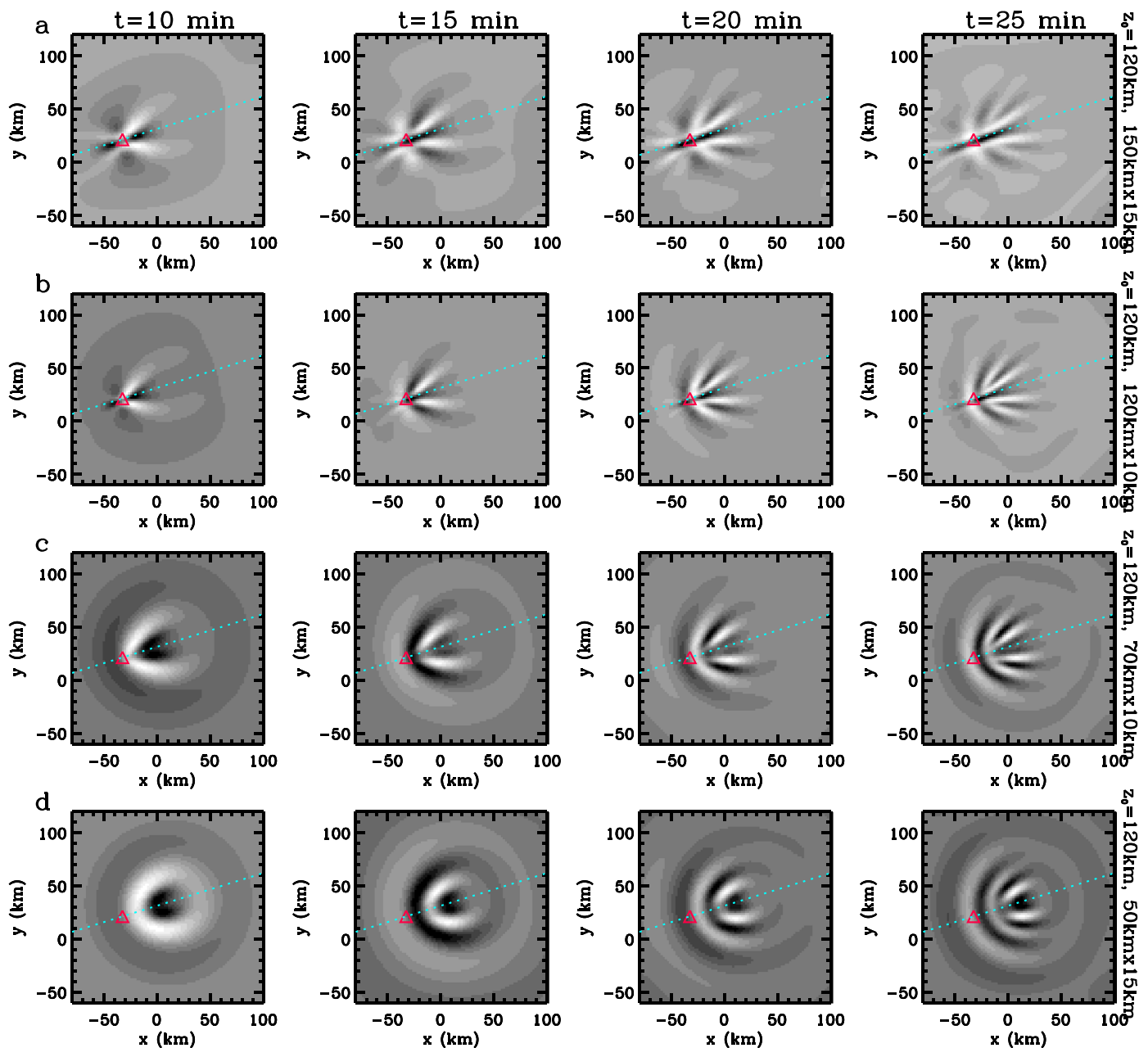


Figure 9. Temperature perturbations at $z = 92$ km associated with the GWs excited by slanted model heatings with $\psi = \psi_{\text{meteor}}$ and $\theta = \theta_{\text{meteor}}$. In each row, we show $t = 10, 15, 20,$ and 25 min from left to right, respectively. (a) $z_0 = 120$ km, $L_{x'} = 150$ km, and $L_{y'} = 15$ km. The maximum values are 7, 4, 3, and 3%, respectively. (b) $z_0 = 120$ km, $L_{x'} = 120$ km, and $L_{y'} = 10$ km. The maximum values are 4, 3, 2, and 2%, respectively. (c) $z_0 = 120$ km, $L_{x'} = 70$ km, and $L_{y'} = 10$ km. The maximum values are 1, 1, 1, and 1%, respectively. (d) $z_0 = 120$ km, $L_{x'} = 50$ km, and $L_{y'} = 15$ km. The maximum values are 1, 1, 1, and 1%, respectively. The blue dotted lines show the meteor trajectory. The red triangles show the observed (estimated) location of the X from Figure 6.

and northeastward propagating GWs (west of the red triangle) have much smaller amplitudes than the southwestward and northwestward propagating GWs (east of the red triangle). Thus, the X is much less pronounced than in Figure 9a.

Figure 9c shows the results for the same model heating as in Figure 9b but with a shorter length of $L_{x'} = 70$ km. The excited GWs have $\lambda_H \sim 30\text{--}40$ km at early times and $\lambda_H \sim 10\text{--}30$ km at later times. Because the heating is shorter, somewhat larger-period GWs are excited. This causes the GWs to travel further horizontally prior to reaching $z = 92$ km, thereby causing the GW phase lines to extend further from the meteor trajectory (up to $\sim 50\text{--}70$ km from the meteor trajectory). Note that there are no southeastward and

northeastward propagating GWs west of the red triangle. Because they would have been created by the portion of the heating below $z = 92$ km, we infer that the heating length of $L_{x''} \sim 70$ km is too short to match the observations.

While many of the general properties of the GWs modeled by Figures 9a–9c agree reasonably well with the observations, there is one which does not. In particular, the observations suggest that λ_H becomes larger in time, while all model results show λ_H becoming smaller in time. This discrepancy may be caused by the background wind which filters out the smaller GWs that have smaller phase speeds at later times or by a more complicated heating profile which widens in time. This latter possibility seems likely, because heat diffusion is expected to widen the heating in time.

Figure 9d shows T'/\bar{T} at $z = 92$ km for a model heating at $z_0 = 120$ km with an even shorter length of $L_{x''} = 50$ km and with a full width of $L_{y''} = 15$ km. Curved GW phase lines are seen which expand outward in time. Because the observations suggest more linearly shaped phase lines, we conclude that $L_{x''}/L_{y''} > 10$, as is the case in Figures 9a and 9b.

Although many of the properties of the GWs in Figures 9a–9c resemble the observations, the GWs in Figures 9a and 9b best resemble the observations because of the presence of the southeastward and northeastward propagating GWs west of the red triangle. In principle, we could use the ratio of the amplitudes of the GWs west and east of the red triangle in Figure 6c to constrain which model best fits the observations. However, we believe that the observations are too noisy to calculate such a ratio confidently. Therefore, we infer a range of best fit full heating lengths of $L_{x''} \sim 120$ –150 km and full heating widths of $L_{y''} \sim 10$ –15 km.

We now study the results of one of the best fit models having $L_{x''} \sim 120$ km (shown in Figure 9b) in more detail. We estimate an (intrinsic) wave period of $\tau_{I_r} \sim 8$ min at $\Delta t \sim 20$ min using results every minute (not shown). Using $\lambda_H \sim 10$ –40 km, we then estimate intrinsic horizontal phase speeds of $c_{IH} \sim 20$ –85 m/s for the GWs east of the red triangle. In this intrinsic frame of reference, the wave properties north and south of the meteor trajectory are identical.

4.1.3. GWs Excited by Slanted Heatings in a Constant Background Wind

We now consider a vertically slanted line-shaped heating in a constant background wind. The resulting solution is quite idealized, because the background wind generally varies substantially throughout the atmosphere. However, such a solution allows for a basic understanding of the effect that the background wind has on the GW structures seen in the airglow images. Therefore, examination of such a solution can be useful.

In Vadas [2013], the initial value solutions were determined for constant zonal and meridional mean winds of U and V , respectively. The heated/forced solutions were only determined for $U = V = 0$ due to the increased difficulty of obtaining a solution [Vadas, 2013]. However, because the heating occurs over a time period of the order of the buoyancy period ($\chi = 5$ min), we can approximate this heating as an initial temperature perturbation instead. We choose an initial temperature perturbation of

$$T'(x, y, z) = T'_0 \exp\left(-\frac{(x'')^2}{2\sigma_{x''}^2} - \frac{(y'')^2}{2\sigma_{y''}^2} - \frac{(z'')^2}{2\sigma_{z''}^2}\right), \quad (26)$$

with an amplitude of $T'_0 = 600$ K. This amplitude is arbitrarily chosen and is not related to the meteor ablation process. (As before, most of this energy goes into mean effects.) Additionally, we choose the same heating parameters as in Figure 9c (i.e., $z_0 = 120$ km, $L_{x''} = 150$ km, and $L_{y''} = 10$ km). The x_0 and y_0 are determined from equation (23). Figures 10a and 10b show the results for a constant southward meridional wind of $V = -10$ m/s at $t = 10$ and 25 min, respectively. (These solutions display equations (C5)–(C6) of Vadas [2013].) We see the expected result; the V-shaped GW structure is Doppler shifted southward from the meteor trajectory, and this shift increases with time. Because the background wind here has no horizontal shear, the overall GW structure is symmetric, similar to Figure 9c. This differs from the observations (see Figure 5). The observations show that c_H is smaller north of the meteor trajectory by ~ 60 m/s as compared to south of this trajectory (see Table 1). The waves north (south) of the meteor trajectory were propagating northwestward (southwestward). This suggests that there was a nonconstant background meridional wind above $z \sim 92$ km at the time of the meteor.

Figures 10c and 10d show the results for a constant westward wind of $U = -20$ m/s. The symmetric GW structure is shifted westward. Figures 10e and 10f show the results for $U = -20$ m/s and $V = -5$ m/s, while

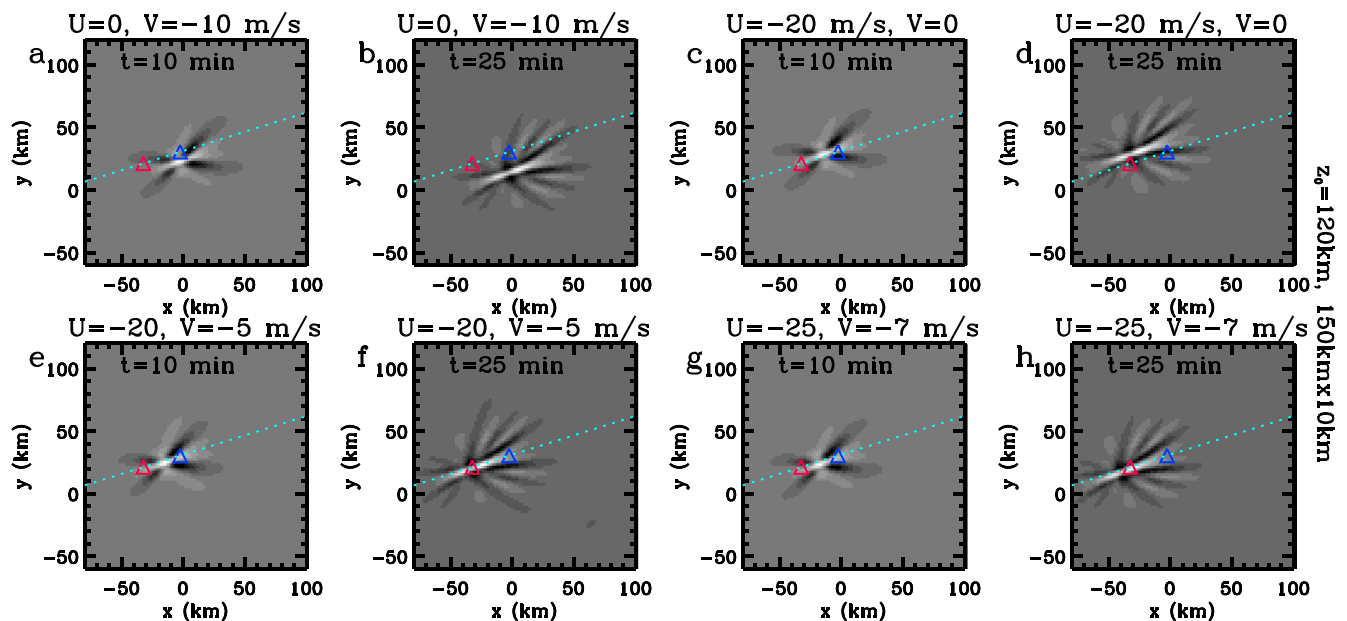


Figure 10. Temperature perturbations at $z = 92$ km associated with the GWs excited by an initial temperature perturbation with $z_0 = 120$ km, $L_x = 150$ km, and $L_y = 10$ km. There is a constant background zonal wind U and/or meridional wind V . (a, b) $t = 10$ and 25 min, respectively, for $U = 0$ and $V = -10$ m/s. (c, d) $t = 10$ and 25 min, respectively, for $U = -20$ m/s and $V = 0$. (e, f) $t = 10$ and 25 min, respectively, for $U = -20$ m/s and $V = -5$ m/s. (g, h) $t = 10$ and 25 min, respectively, for $U = -25$ m/s and $V = -7$ m/s. The maximum values in Figures 10a–10h are 18, 10, 18, 10, 17, 10, 18, and 10%, respectively. The blue dotted lines show the meteor trajectory. The blue triangles show the assumed location of the meteor at $z = 92$ km. The red triangles show the observed location of the X.

Figures 10g and 10h show the results for $U = -25$ m/s and $V = -7$ m/s. For these latter two cases, the GW structure and X are shifted southwestward along the meteor trajectory. The southwest offset of the X in the Na airglow observations, therefore, could be caused by a southwestward background wind at $z = 92$ km (see section 4.1.2).

Suzuki *et al.* [2013] determined the background wind profile from $z = 76$ to 87 km by examining the movement of the circular train (created by this meteor) in time [Suzuki *et al.*, 2013, Figure 5]. Although they did not determine the background wind at $z = 92$ km (because the meteor train above 87 km was too faint), the background wind contained a wave (likely an inertial GW) with a vertical wavelength of ~ 14 – 16 km. Extrapolating the wind perturbation from this wave upward in altitude, the background wind at $z \sim 92$ km may have been northwestward, because the wind at $z = 78$ km was northwestward. However, this extrapolation is prone to error, because the background wind at $z = 92$ km would have also been influenced by other waves and/or by wave breaking. Therefore, it is possible that the wind at $z = 92$ km was southwestward.

Finally, we note that variable wind and wind shear above $z = 92$ km were not taken into account in our modeling results. Ray trace or other numerical studies (which are outside the scope of this paper) would need to be performed to better understand the effects of the background wind on the structure of these GWs.

4.1.4. AWs Excited by a Vertically Slanted, Line-Shaped Heating in Zero Wind

We now calculate the AWs excited by the heating shown in Figure 9b in an atmosphere with zero background winds: $U = V = 0$. Figure 11 shows only the AWs at $z = 92$ km at $\Delta t = 1, 2, 3,$ and 4 min. The AWs consist of arc-like waves that appear to propagate away from the horizontal projection of the meteor trajectory. Each wave contains primarily a single plus/minus sinusoidal oscillation. South of the meteor trajectory, the AWs have an average horizontal phase speed of ~ 240 – 280 m/s, which is slightly smaller than the sound speed ($c_s = 282$ m/s).

4.2. GWs Excited by a Slanted, Line-Shaped Body Force in Zero Wind

In this section, we calculate the GWs excited by a vertically slanted, line-shaped 3-D body force (i.e., 3-D acceleration) for completeness. We present the solution for a force that is slanted along the direction of the meteor trajectory. Our motivation for performing this simulation is as follows. As the meteor ablates in the MLT region, the molecules within the meteor interact and collide with the neutral gas molecules

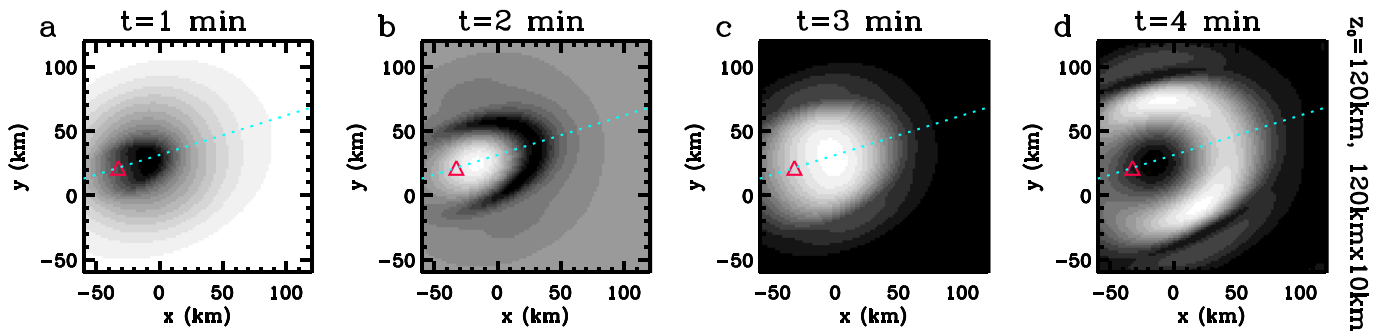


Figure 11. Temperature perturbations at $z = 92$ km associated with the AWs excited by a slanted model heating with $z_0 = 120$ km, $L_{x''} = 120$ km, and $L_{y''} = 10$ km. (a–d) $t = 1, 2, 3,$ and 4 min, respectively. The maximum values are $0.03, 0.01, 0.03,$ and 0.02% , respectively. The blue dotted lines show the meteor trajectory. The red triangles show the observed location of the X.

in the vicinity of the meteor. The net effect is that these molecules are accelerated in the direction of the meteor. However, because the meteor was likely small (baseball-sized), the momentum imparted to the fluid was likely small. Therefore, we do not expect this mechanism to be the main generator of GWs from meteor ablation.

Similar to the heatings in section 4.1, we model the spatial portion of the 3-D body force as a Gaussian in space which is oriented θ counterclockwise from east and ψ from the horizontal. We translate and rotate the coordinate system to the center of the body force using equations (19)–(21). Our model 3-D body force is

$$\mathbf{F}(\mathbf{x}) = F_0 \exp\left(-\frac{(x'')^2}{2\sigma_{x''}^2} - \frac{(y'')^2}{2\sigma_{y''}^2} - \frac{(z'')^2}{2\sigma_{z''}^2}\right) \left[(\cos\theta \cos\psi) \hat{\mathbf{i}} + (\sin\theta \cos\psi) \hat{\mathbf{j}} + (\sin\psi) \hat{\mathbf{k}} \right], \quad (27)$$

where F_0 is the maximum amplitude, $\hat{\mathbf{i}}, \hat{\mathbf{j}},$ and $\hat{\mathbf{k}}$ are the unit vectors in the zonal, meridional, and vertical geographic directions, respectively, and (x_0, y_0, z_0) is the center of the body force. The x_0 and y_0 are determined from equation (25). We choose $F_0 = 300$ m/s. This amplitude is arbitrarily chosen and is not related to the meteor ablation process.

Figure 12 shows the temperature perturbations associated with the GWs at $z = 92$ km for this model force in an atmosphere with zero background winds: $U = V = 0$. Here we choose the same parameters as in Figure 9b: $z_0 = 120$ km, $L_{x''} = 120$ km, and $L_{y''} = 10$ km. The largest-amplitude GWs are located east of the red triangle and have a V-shaped structure. Of these GWs, those south of the meteor trajectory propagate southwestward, while those north of the meteor trajectory propagate northwestward. The phase lines end abruptly at the blue dotted line, giving the appearance that the GWs originate along the horizontal projection of the meteor trajectory. These GWs have similar scales and periods as those GWs excited by the model heating with the same length and width (i.e., Figure 9b). For the application of meteor ablation, a more detailed study would need to be performed to understand the importance of this excitation mechanism as compared to the vertically slanted heating.

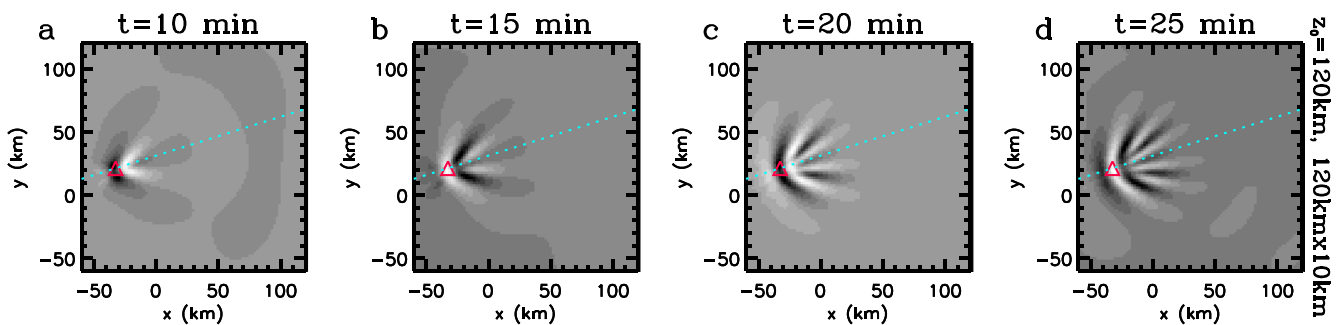


Figure 12. Temperature perturbations at $z = 92$ km associated with the GWs excited by a slanted model 3-D body force with $z_0 = 120$ km, $L_{x''} = 120$ km, and $L_{y''} = 10$ km. (a–d) $t = 10, 15, 20,$ and 25 min, respectively. The maximum values are $1.0, 0.8, 0.5,$ and 0.4% , respectively. The blue dotted lines show the meteor trajectory. The red triangles show the observed location of the X.

5. Discussion

In section 3, we presented observations of faint GWs which appeared to be colocated in time with the passage of a fireball meteor and appeared to radiate from the horizontal projection of the meteor trajectory. The wave phase lines converged at the location of this horizontal projection, at an angle from this trajectory. We then presented model results of slanted heatings and a 3-D body force aligned along the meteor trajectory in section 4 and found that both excite GWs similar to the structures seen in the observations. We focused on heatings, which are the most likely mechanism for wave generation in the vicinity of the meteor trajectory. We found that in order to compare well with the observations, it was necessary for the center of the heating to be located well above the Na airglow layer (at $z \sim 120$ km), which is above the assumed altitude where the luminosity function peaks ($z \sim 88$ km). However, the altitude where the neutrals are maximally heated is likely different from the altitude where the ionized molecules maximally emit light. Additionally, we found that this modeled heating needed to have a full length of ~ 120 – 150 km and a full width of ~ 10 – 15 km. These values are equivalent to a half-length half maximum of $\sigma_{x''} \sim 25$ – 35 km and a half width half maximum of $\sigma_{y''} = \sigma_{z''} \sim 2$ – 3 km.

It is well known that bright meteors generate infrasonic pressure waves, which are sometimes audible on the ground [Revelle, 1976]. The radius of the cylindrical blast wave produced by a line-source sound-generating region around a meteor is given by approximately [Revelle, 1976]

$$R_0 \approx Md_m, \quad (28)$$

where M is the Mach number of the meteor and d_m is the meteor diameter. M for the observed meteor is $\gg 1$. Using a local sound speed of $c_s \sim 282$ m/s, we estimate $M \sim 245$. Although its size and mass are unknown, the meteor is classified as a fireball meteor because its apparent magnitude is brighter than -4 (see Figure 1d). The radius of a fireball meteor is generally thought to be at least 10 cm. Therefore, we conservatively choose a radius of 10 cm [Ceplecha et al., 1998]. We then estimate a blast wave radius at $R_0 \sim 50$ m. At lower altitudes, as a significant fraction of the meteor's mass is ablated, the blast wave radius will reduce or the meteor will fragment. Revelle [1976] also showed that the frequency of the acoustic wave is expected to be $\sim c_s/R_0 \sim 5.6$ Hz or a period of ~ 0.18 s. The wavelength of the near-field shock wave is expected to be ~ 140 m. Because of the high frequency of this wave, heat conduction and molecular viscosity effectively damp this wave [Ceplecha et al., 1998].

The shock wave likely causes heating within a few wavelengths until it is fully dissipated, a process which depends on the local heat conduction and viscosity and thus varies strongly with altitude. We estimate the total region affected by the shock heating via (1) assuming that the shock causes rapid atmospheric heating over a few hundred meters, and (2) that heat diffuses radially outward from the line source over longer time scales. We estimate the heat diffusion via solving a transient heat diffusion equation:

$$\frac{\partial T'(\mathbf{r}, t)}{\partial t} - D \nabla^2 T'(\mathbf{r}, t) = f(\mathbf{r}, t), \quad (29)$$

where T' is the temperature perturbation, $D = k/\rho C_p$ is the thermal diffusivity, ρ is the density, k is the thermal conductivity, C_p is the specific heat at constant pressure, $f(\mathbf{r}, t)$ is the heat deposition, and \mathbf{r} is the radius. An analytical Green's function solution to this equation for the case of a line-shaped Gaussian heating ($\propto \exp[-(x^2 + y^2)/2\sigma^2]$) where σ is the Gaussian width of the heating and $r^2 = x^2 + y^2$ is the distance from the line heating source) has been given by Antonakakis et al. [2013]:

$$T'(r, t) = -\frac{A \sigma^2}{2k} \left[\text{Ei}\left(1, \frac{r^2}{2\sigma^2}\right) - \text{Ei}\left(1, \frac{r^2}{2\sigma^2 + 4Dt}\right) \right], \quad (30)$$

where A is the power density of the forcing, and $\text{Ei}(1, z) = \int_1^\infty (1/t)e^{-tz} dt$ is the exponential integral. Using values from the empirical NRLMSIS model [Hedin, 1991] for $z = 110$ km (i.e., $\rho \sim 8.5 \times 10^5$ g/m³, $T_0 = 224$ K), we estimate the thermal diffusivity to be $D \sim 262$ m²/s at this height. After solving equation (30), we find that after 5 min a region with $\sigma = 400$ m will diffuse to a radius of 1.5–2 km. This scale size is in rough agreement with the modeled heating half width needed to approximate the observations (i.e., $\sigma_{y''} = \sigma_{z''} \sim 2$ – 3 km). We note that there are many unknowns in the heating and diffusion processes; these estimates are simply meant to illustrate that the heated volume from the meteor shock wave could diffuse to kilometer scales over time scales associated with GW generation. We also note that the preceding discussion does not account for the rapid increase in D with height.

6. Conclusions

In this paper, we presented Na airglow observations at Syowa Station, Antarctica, on 7 June 2008 following the passage of a fireball meteor. This southwestward moving meteor entered the atmosphere above Syowa Station at 21:58:45 UT [Suzuki *et al.*, 2013]. Whereas the companion paper focused on extracting the background horizontal winds from the movement of the circular train in the early images ($\Delta t = 2\text{--}9$ min after the meteor) [Suzuki *et al.*, 2013], this paper focused on identifying and understanding the V-shaped faint waves observed in the Na images $\Delta t = 8\text{--}43$ min after the meteor. Here $\Delta t = 0$ denotes the time the meteor was observed. Because the aurora was quite strong, these faint waves were only observed $\sim 50\%$ of the time, and even then only portions of the wave phase lines were generally visible.

These waves were identified as GWs because their periods were somewhat larger than the buoyancy period and because they moved in a direction perpendicular to their phase lines. These phase lines were straight, not curved, and appeared to originate from (i.e., end abruptly at) the horizontal projection of the meteor trajectory to $z = 92$ km. The phase lines of these GWs appeared to form an X centered on the meteor trajectory, with the larger-amplitude GWs forming Vs whose open ends pointed toward the northeast. Smaller amplitude, fainter GWs appeared to form oppositely directed Vs.

Approximately east of the location where the meteor crossed the altitude $z = 92$ km (dubbed the meteor crossing altitude), the waves south of the path propagated southwestward with an observed horizontal phase speed of $c_H \sim 80\text{--}100$ m/s, while those north of the path propagated northwestward with $c_H \sim 20\text{--}40$ m/s. Additionally, those GWs south of the path had horizontal wavelengths $\lambda_H \sim 25\text{--}35$ km and periods $\tau_r \sim 5\text{--}6$ min, while those north of the path had $\lambda_H \sim 18$ km and $\tau_r \sim 7\text{--}15$ min. The angle of the GW phase lines with respect to the meteor trajectory was $-(42\text{ to }52)^\circ$ for the GWs south of the path and $(10\text{ to }20)^\circ$ for the GWs north of the path. These values varied slowly in time and were classified according to "early" times ($\Delta t = 8\text{--}16$ min) and "late" times ($\Delta t = 28\text{--}43$ min) (see Table 1).

We then presented model results for the GWs and AWs excited by idealized heatings and a 3-D body force using linear, compressible solutions. Note that because we ultimately found that $|\lambda_z| < \pi H$ for the excited GWs, we could have used the Boussinesq solutions from Vadas and Fritts [2001] instead of the compressible solutions to calculate the excited GWs. However, this result was not obvious, because the vertical extent of the slanted heating was much larger than H . (Additionally, the compressible solutions were needed to calculate the excited AWs.)

Using the Vadas [2013] compressible model, we first determined the GWs excited by a horizontally aligned (i.e., zero slant) line-shaped heating in zero wind. These GWs propagated away from the heating with phase lines parallel to the heating direction. We then showed the GWs excited by a short-length heating that was slanted along the direction of the meteor trajectory. If this heating was located at $z < 92$ km, a V-shaped GW structure was formed at $z = 92$ km west of the meteor crossing altitude. The open end of this V pointed toward the southwest and was formed by upward propagating GWs. If this heating was located at $z > 92$ km, a V-shaped GW structure was formed at $z = 92$ km east of the meteor crossing altitude. In this case, the open end of the V pointed toward the northeast and was formed by downward propagating GWs excited at higher altitudes. We then modeled a longer heating and found that if its center was located at $z > 92$ km, the largest-amplitude GWs were created east of the meteor crossing altitude in a V-shaped structure, with the open end of the V facing the northeast. If there was also significant heating at $z < 92$ km, then smaller-amplitude GWs were also created west of the meteor crossing altitude in a V-shaped structure with the open end of the V facing the southwest. In this latter case, the conjunction of the northeast and southwest facing Vs created an X structure. The center of this X was located at the observation altitude (i.e., at $z = 92$ km). The structure created from this heating was most similar to the observations. Therefore, we concluded that the center of the meteor-induced heating was located at $z_0 > 92$ km and that this heating was long and extended somewhat below $z = 92$ km.

We found from our modeling results that the center of the X is located at the observation altitude if the background winds are 0. We determined the center of the X from the Na airglow images and found that this location was different from the location using the assumed meteor trajectory at $z = 92$ km (from the ATV). This could have occurred if the assumed altitude for the meteor was ~ 17 km lower than the actual altitude. This is unlikely, however, because it leads to an unrealistically large geocentric meteor velocity. The most likely possibility was that there was a southwest background wind at $z = 92$ km which shifted the GW

structure southwestward in the Na airglow images. We demonstrated that this could occur for a constant southwest wind of ~ 20 m/s.

We then varied z_0 , the length, and the width of this slanted heating in order to determine the model parameters which most closely resembled the Na airglow observations. If z_0 was too close to $z = 92$ km, the GW phase lines did not extend more than ~ 30 km south of the meteor trajectory. This is because the excited GWs have very high frequencies, which cause GW propagation over similar horizontal and vertical distances [Fritts and Alexander, 2003] (i.e., a vertical propagation distance of 20–30 km occurs simultaneously with a horizontal propagation of distance of ~ 20 –30 km if the wave period is approximately equal to the buoyancy period). In order to be more consistent with the Na airglow observations (since the GWs phase lines are observed ~ 50 –70 km south of the meteor trajectory), we found that the heating center needed to be located at $z_0 \sim 120$ km. We then varied the heating widths. We found that a full width (or diameter) of $L_{y''} = L_{z''} \sim 10$ –15 km (i.e., radial width of 5–7.5 km) resulted in GWs with $\lambda_H \sim 10$ –40 km, consistent with the observations. Smaller (larger) widths resulted in GWs with smaller (larger) λ_H . We then varied the heating lengths. If the full length was too short ($L_{x''} \sim 50$ km), the GW phase lines were curved rather than straight, yielding concentric “arc-like” ring structures at $z = 92$ km instead. Additionally, the southwest pointing V (west of the meteor crossing altitude) and the X structure were not created. We found that a full length of $L_{x''} \sim 120$ –150 km best fit the observations. Similar results were obtained for a slanted 3-D body force, although it is likely that the heating created by this meteor is more important than the slanted body force created by this meteor. We also calculated the AWs excited by the best fit heating. The AWs were arc-like, propagated away from the meteor trajectory, and had horizontal phase speeds of ~ 240 –280 m/s. Each wave consisted primarily of a single plus/minus sinusoidal oscillation.

In conclusion, the best fit heating parameters for this meteor event were found to be a central altitude of $z_0 \sim 120$ km, half-length half maximum of $\sigma_{x''} \sim 25$ –35 km, and half width half maximum (i.e., half maximum radius) of $\sigma_{y''} = \sigma_{z''} \sim 2$ –3 km. We note that we found the center of this heating, z_0 , to be located well above $z = 92$ km even though the luminosity function likely peaked at $z \sim 88$ km. This is not surprising, because the altitude where the neutrals peak need not correspond to the altitude where the ionized molecules maximally emit light. The half-length half maximum $\sigma_{x''}$ makes sense, because it is similar to the half-length half maximum of the luminosity function (although with the same caveat as above). We then argued that the half-width half maximum $\sigma_{y''} = \sigma_{z''}$ also made sense as follows. We estimated the radius of the initial blast (shock) wave to be 50 m for this fireball meteor, with a shock wave wavelength of 140 m. Assuming that it took several wavelengths to fully dissipate, we estimated a shock dissipation radius of ~ 400 m. We then solved the cylindrical heat diffusion equation and found that after ~ 5 min, diffusion would have occurred out to a radius of 1.5–2 km. This is the estimated “half maximum” radius of the heating that would result from this meteor and is consistent with our best fit modeled half width half maximum of $\sigma_{y''} = \sigma_{z''} \sim 2$ –3 km.

Acknowledgments

S.L.V. was supported by NSF grants ATM-0836195 and AGS-1139149. T.N. and H.S. were supported by JSPS grant 24340121 and NIPR Project Research KP-2. The Syowa ASI is operated by the Science Program of JARE supported by NIPR, under MEXT, Japan. M.J.N. was supported by NSF grant AGS-1139152. The data shown in this paper may be available for collaborative research pending an e-mail request to the authors.

References

- Alexander, M. J., J. R. Holton, and D. R. Durran (1995), The gravity wave response above deep convection in a squall line simulation, *J. Atmos. Sci.*, *52*(12), 2212–2226, doi:10.1175/1520-0469.
- Antonakakis, T., C. Maglioni, and V. Vlachoudis (2013), Closed form solutions of the heat diffusion equation with a Gaussian source, *Int. J. Heat Mass Transfer*, *62*, 314–322, doi:10.1016/j.ijheatmasstransfer.2013.02.061.
- Birney, D. S., G. Gonzalez, and D. Oesper (2006), *Observational Astronomy*, 2nd ed., Cambridge Univ. Press, Cambridge, U. K.
- Carroll, B. W., and D. A. Ostlie (2006), *An Introduction to Modern Astrophysics*, 2nd ed., Pearson Addison-Wesley, San Francisco, Calif.
- Ceplecha, Z., J. Borovička, W. G. Elford, D. O. Revelle, R. L. Hawkes, V. Porubcan, and M. Šimek (1998), Meteor phenomena and bodies, *Space Sci. Rev.*, *84*, 327–471.
- Chromey, F. R. (2010), *To Measure the Sky: An Introduction to Observational Astronomy*, Cambridge Univ. Press, Cambridge, U. K.
- Cousins, A. W. J. (1971), “Photometric Standard Stars”, Royal Observatory Annals, No. 7, Royal Greenwich Observatory.
- Greer, R. G. H., and G. T. Best (1967), A rocket-borne photometric investigation of the oxygen lines at 5577 and 6300, the sodium D-lines and the continuum at 5300 in the night airglow, *Planet. Space Sci.*, *15*(12), 1857–1881.
- Fritts, D. C., and M. J. Alexander (2003), Gravity wave dynamics and effects in the middle atmosphere, *Rev. Geophys.*, *41*, 1003, doi:10.1029/2001RG000106.
- Hedin, A. E. (1991), Extension of the MSIS thermosphere model into the middle and lower atmosphere, *J. Geophys. Res.*, *96*, 1159–1172.
- Hocke, K., and K. Schlegel (1996), A review of atmospheric gravity waves and traveling ionospheric disturbances, *Ann. Geophys.*, *14*, 917–940.
- Holton, J. R., and M. J. Alexander (1999), Gravity waves in the mesosphere generated by tropospheric convection, *Tellus B*, *51*, 45–58.
- Liseau, R., et al. (2013), “ α Centauri A in the far infrared. First measurement of the temperature minimum of a star other than the Sun”, *Astron. Astrophys.*, *549*, L7.
- Revelle, D. O. (1976), On meteor-generated infrasound, *J. Geophys. Res.*, *81*(7), 1217–1230.
- Richmond, A. D. (1978), Gravity wave generation, propagation, and dissipation in the thermosphere, *J. Geophys. Res.*, *83*, 4131–4145.
- Söderhjelm, S. (1999), Visual binary orbits and masses post Hipparcos, *Astron. Astrophys.*, *341*, 121–140.

- Suzuki, H., Y. Tomikawa, M. Taguchi, T. Nakamura, and M. Tsutsumi (2010), Variations of OH rotational temperature over Syowa Station in the austral winter of 2008, *Earth Planets Space*, *62*, 655–661.
- Suzuki, H., T. Nakamura, S. L. Vadas, M. Tsutsumi, M. Taguchi, and Y. Fujiwara (2013), Inertia-gravity wave in the polar mesopause region inferred from successive images of a meteor train, *J. Geophys. Res. Atmos.*, *118*, 3047–3052, doi:10.1002/jgrd.50228.
- Taguchi, M., M. Ejiri, and K. Tomimatsu (2004), A new all-sky optics for aurora and airglow imaging, *Adv. Polar Upper Atmos. Res.*, *18*, 140–148.
- Vadas, S. L. (2013), Compressible f-plane solutions to body forces, heatings, and coolings, and application to the primary and secondary gravity waves generated by a deep convective plume, *J. Geophys. Res. Space Physics*, *118*, 2377–2397, doi:10.1002/jgra.50163.
- Vadas, S. L., and D. C. Fritts (2001), Gravity wave radiation and mean responses to local body forces in the atmosphere, *J. Atmos. Sci.*, *58*, 2249–2279.
- Vadas, S. L., D. C. Fritts, and M. J. Alexander (2003), Mechanism for the generation of secondary waves in wave breaking regions, *J. Atmos. Sci.*, *60*, 194–214.
- Vadas, S. L., J. Yue, C.-Y. She, P. A. Stamus, and A. Liu (2009), A model study of the effects of winds on concentric rings of gravity waves from a convective plume near Fort Collins on 11 May 2004, *J. Geophys. Res.*, *114*, D06103, doi:10.1029/2008JD010753.
- Walterscheid, R. L., G. Schubert, and D. G. Brinkman (2001), Small-scale gravity waves in the upper mesosphere and lower thermosphere generated by deep tropical convection, *J. Geophys. Res.*, *106*(D23), 31,825–31,832.
- Yue, J., S. L. Vadas, C.-Y. She, T. Nakamura, S. C. Reising, H.-L. Liu, P. Stamus, D. A. Krueger, W. Lyons, and T. Li (2009), Concentric gravity waves in the mesosphere generated by deep convective plumes in the lower atmosphere near Fort Collins, Colorado, *J. Geophys. Res.*, *114*, D06104, doi:10.1029/2008JD011244.
- Zhu, X., and J. R. Holton (1987), Mean fields induced by local gravity-wave forcing in the middle atmosphere, *J. Atmos. Sci.*, *44*, 620–630.